THESIS

SEISMIC ANISOTROPY IN NORTHWESTERN CANADA AND EASTERN ALASKA FROM SHEAR WAVE SPLITTING MEASUREMENTS

Submitted by

Derek Richard Witt

Department of Geosciences

In partial fulfillment of the requirements

For the Degree of Master of Science

Colorado State University

Fort Collins, Colorado

Fall 2017

Master's Committee:

Advisor: Derek Schutt

Richard Aster
Jay Breidt

ABSTRACT

SEISMIC ANISOTROPY IN NORTHWESTERN CANADA AND EASTERN ALASKA FROM SHEAR WAVE SPLITTING MEASUREMENTS

The Mackenzie Mountains are an actively uplifting and seismogenic mountain range that lies within the Yukon and Northwest Territories, Canada. The range is an eastward salient of the complexly deformed northern Canadian Cordillera, and lies ~500 kilometers away from and significantly off axis of the convergence direction of the Yakutat Indentor, a small oceanic-continental terrane that is subducting northward under North America in the Gulf of Alaska. To better assess the causes of the Mackenzie Mountains uplift and its broader relationship to deformation within the Northern Canadian Cordillera, shear wave splitting measurements have been performed on seismometers at over 150 locations within this region. Many of the measurements come from the Mackenzie Mountains Earthscope Project, a ~900 km NE-directed transect that spans from the complexly deformed coastal ranges near Skagway, Alaska, across the shortening axis of the Mackenzie Mountains, to the cratonic lithosphere at Great Bear Lake. This array is the first deployment of broadband seismometers within the Mackenzie Mountains and the current study is the first report from that array. Shear wave splitting provides a means to probe the seismic velocity anisotropy, and therefore the strain history, of the lithosphere and asthenosphere. Results indicate five distinct subregions of splitting behavior in our results: 1) chaotic, non-uniform splitting in the subduction zone complex; 2) fault-parallel fast axes along and between the Denali and Tintina dextral fault systems; 3) a short section of east-west fast axes near the British Columbia-Yukon border; 4) consistent fast axes aligned with North America

absolute plate motion within the Canadian shield; and 5) the transitional inboard region between the Tintina fault and the Canadian shield, which includes the Mackenzie Mountains. Our findings support the hypothesis that shear from the Tintina and Denali faults penetrates the lithospheric mantle and has produced significant lithospheric anisotropy. The location of the strained mantle causing the observed anisotropy transitions from the lithosphere near the subduction zone and transpressional fault systems to the asthenosphere in the Canadian shield, where observations of asthenospheric flow are consistent with North America absolute plate motion.

ACKNOWLEDGEMENTS

First and foremost, I would like to thank Derek Schutt for giving me the opportunity to work on the Mackenzie Mountains research project and to perform this research. His guidance and friendship was instrumental in the successful completion of my Master's program. I'd like to thank Rick Aster for insightful conversations about geophysical ideas and methods and for the great times in the field. I owe a huge thank you to Jay Breidt, who helped me immensely with understanding the mathematical concepts behind our shear wave splitting method and also taught me the intricacies of R. I thank my fellow graduate students, past and present, for their friendship and after-hours guidance. Most importantly, I'd like to thank my wife, Emily, for her never ending encouragement and support during graduate school. Lastly, I'm very grateful for the funding of this project that was provided by Dr. Schutt and NSF Grant EAR-1460533.

TABLE OF CONTENTS

LIST OF TABLES

LIST OF FIGURES

CHAPTER 1

1.1 Organization of Thesis

The following master's thesis is formatted into three chapters. *Chapter One* provides the background information for the project, which includes information on seismic velocity anisotropy, shear wave splitting, and the shear wave splitting methodology used herein. *Chapter Two* is structured as a technical manuscript that is to be refined and submitted to a peer-reviewed geophysics journal. Thus, it will cover the shear wave splitting results and discussion for the northern North American Cordillera in both scientific and statistical contexts. Because *Chapter Two* is meant to be a self-containing journal article, some information such as *Results* and *Discussion* is stated solely in that chapter. *Chapter Three* includes propositions for future work along with data acquisition and processing information. This chapter is aimed at future graduate students or researchers who wish to build upon this work.

1.2 Overview of Project

This body of work presents shear wave splitting results for the northern North American Cordillera and surrounding area via a new shear wave splitting technique. The results obtained herein can be utilized as a basis for further hypothesis testing since the aforementioned method is the first of its kind to produce formal statistical uncertainties. This research was undertaken with the goal of better understanding the northern North American Cordillera strain history along with forming a basis for future multiple-layer anisotropy studies. A secondary result of this study is the production of scripts and methods that optimize the user time and input required to screen good seismograms and to get robust station averages of shear wave splitting parameters. These

can provide a foundation for future graduate students and/or researchers who are at the beginning stages of a shear wave splitting study.

1.3 Seismic Velocity Anisotropy

Seismic anisotropy is a commonly used shorthand for seismic velocity anisotropy, which is the dependence of elastic wave velocity on propagation direction. An anisotropic elastic system (e.g., the upper mantle) can be generally characterized by its elasticity tensor. The elasticity tensor is a fourth-order tensor that relates the second order stress tensor to the second order strain tensor and, with density, provides the information needed to calculate directionally-dependent seismic wave velocities. Although there are 81 terms in a fourth order tensor, symmetry reduces the total number of unique terms to 21. Often in the case of shear wave splitting, hexagonal symmetry is assumed, which reduces the number of free terms in the elasticity tensor to 6. Given a direction of wave propagation and an elasticity tensor, one can generate the 3x3 Christoffel matrix to find the phase velocities and wave polarizations along an arbitrary direction. The three eigenvalues of the Christoffel matrix give the wave speeds, and the eigenvector corresponding to each eigenvalue gives the polarization of the wave that travels at each wave speed.

Some of the first work on earth-relevant anisotropy was produced by *Turner* [1942], who showed that olivine crystals develop a preferred orientation during deformation. Later the seismic velocities of olivine crystallographic axes were measured [*Verma*, 1960]. *Hess* [1964] tied seismic observations to olivine fabric by solving for directional dependence of P wave velocity in the uppermost oceanic mantle, and noting the presence of lattice preferred orientation of olivine in a sample taken elsewhere at an oceanic core complex.

Many authors since *Hess* [1964] have shown that upper mantle anisotropy is caused by the deformation-induced lattice preferred orientation (LPO; referred to as crystalline preferred orientation (CPO) in some literature) of the abundant upper mantle minerals, olivine and orthopyroxene (Figure 1.1) [e.g., *McKenzie*, 1979; *Nicolas and Christensen*, 1987; *Silver and Chan*, 1991]. LPO textures are created when crystals within a polycrystalline aggregate are preferentially aligned by an externally imposed deformation mechanism [e.g., *Di Leo et al.*, 2014]. Dislocation creep is commonly presumed to be the dominant mechanism for LPO fabric [*Mainprice et al.*, 2000; *Karato et al.,* 2008; *Long and Silver*, 2009], although additional deformation mechanisms such as grain boundary sliding, dislocation glide, and diffusion creep may also play a role in upper mantle anisotropy origination [*Di Leo et al.,* 2014]. However, there is skepticism about the influence of diffusion creep on LPO fabric [*McKenzie*, 1979], and it has long been shown that it can erase preexisting fabric [*Ashby and Verrall*, 1973, *Long and Silver*, 2009]. Olivine is the principal upper mantle component [e.g., *Frost*, 2008], and xenolith studies show that for typical mantle conditions it contributes the most to seismic anisotropy [*Zhang and Karato*, 1995]; therefore, it is usually assumed that olivine LPO is the primary source of observed anisotropy [*Silver and Chan*, 1991; *Zhang and Karato*, 1995; *Silver*, 1996]. LPO in the upper mantle is thought to be a result of the mantle's convection processes and therefore is perhaps the most direct method for constraining mantle flow and dynamics [*Silver and Chan*, 1991; *Long and Becker*, 2010]. Although LPO is thought to be the primary cause of observed anisotropy, shape preferred orientation (SPO) of materials with isotropic elastic properties (e.g., layers of partial melt) may also contribute in certain circumstances [*Long and Becker*, 2010].

Numerous anisotropy studies have aimed to understand how features such as subduction zones, mid-ocean ridges, and mantle plumes affect the LPO of olivine [*Zhang and Karato*, 1995;

Kaminski et al., 2004; *Karato et al.*, 2008; *Long*, 2013]. Partial melting, as well as variations in water, stress, temperature, and pressure, can lead to as many as five different types of olivine LPO [*Karato et al.*, 2008]. The influence of water and stress on olivine LPO are the principal factors, although changes in temperature, pressure, and the onset of partial melting can each cause the redistribution of water, making these secondary factors quite important [*Karato et al.*, 2008].

Investigating seismic anisotropy can also shed light on frozen lithospheric deformation [e.g., *Crampin*, 1984; *Hanna and Long*, 2012]. When averaging many events at a given station, it has been shown that results are biased towards the much thicker layer of anisotropic mantle [e.g., *Bormann et al.*, 1996] but perturbations in the measured delay times and polarization directions have been used to infer additional layers of anisotropy in the lower crust [*Levin et al.*, 1999; *Hanna and Long*, 2012]. This anisotropy is commonly thought to be a result of paleo-strain from orogenic processes [e.g., *Levin et al.*, 1999], or the suturing of exotic terranes proximal to subduction margins [e.g., *Christensen and Abers*, 2010].

Although not studied here, seismic anisotropy can also be observed in other regions within the earth, such as the transition zone [e.g., *Karato et al.*, 1998], the lower mantle and D" layer [e.g., *Kendall and Silver*, 1996], and the inner core [e.g., *Morelli et al.*, 1986].

1.4 Shear Wave Splitting

The most frequently used technique to characterize solid earth anisotropy is shear wave splitting. This phenomenon is analogous to optical birefringence and occurs when a seismic shear wave encounters an anisotropic medium (e.g., LPO fabric of olivine). Upon encountering the medium, the shear wave is split into two orthogonally polarized waves travelling at different velocities, with the faster wave typically following the dominant direction of anisotropy (in the

case of hexagonal symmetry) and the slower, orthogonal wave, lagging behind [e.g., *Silver*, 1996; *Long and Becker*, 2010]. The two parameters often used to quantify anisotropy from shear wave splitting are called the fast axis orientation (ϕ) and the split time (δt), which refer to the polarization direction of the first-arriving "fast" split shear wave and the time lag between the two polarized shear waves, respectively. The fast axis orientation is sensitive to the geometry of the anisotropic fabric and the split time is proportional to the thickness and intensity of the anisotropic fabric (Figure 1.2) [*Silver and Chan*, 1991; *Menke and Levin*, 2003]. For simple systems, these two parameters give the general direction and intensity of anisotropy in a given region.

The most commonly used seismic wave phases used for shear wave splitting analysis are SKS, SKKS, and PKS (hereafter grouped as XKS), which are core-refracted phases (Figure 1.3) [*Long and Becker*, 2010]. Teleseismic core-refracted seismic waves offer a unique constraint on source-side anisotropy because they are radially polarized when they are converted from a compressional (P) wave to a shear (S) wave at the core-mantle boundary (CMB). This radial polarization at the CMB removes all source-side effects and constrains any observed anisotropy to the receiver-side of the ray path [*Silver and Chan*, 1991; *Long and Becker*, 2010]. Additionally, XKS phases travel in a nearly vertical manner through the mantle, which simplifies the analysis but makes it difficult to resolve the depth at which the measured anisotropy is occurring [*Long and Silver*, 2009].

XKS waves are primarily observed on the horizontal channels of a seismometer because these phases follow ray paths that are nearly vertical near the surface (Figure 1.3). For shear wave splitting, the horizontal channels are typically rotated into the radial (R) and tangential (T) directions, which refer to the direction from the receiver to the earthquake and the perpendicular

to this direction, respectively (Figure 1.4). In the presence of a single layer of horizontally-oriented anisotropy, the effects of shear wave splitting on a vertically incident wave with source function, s(t), as recorded on the R(t) and T(t) channels will be:

$$R(t) = s(t)\,cos^2\phi + s(t - \delta t)\,sin^2\phi \qquad \text{(Eqn. 1.4.1)}$$

$$T(t) = \left[\frac{s(t) - s(t - \delta t)}{2}\right] sin2\phi \qquad \text{(Eqn. 1.4.2)}$$

where ϕ is the angle between the radial direction and fast axis and δt is the split time [*Stein and Wysession*, 2012]. This effect is observed when the anisotropic layer is significantly larger than the wavelength of the seismic wave (i.e., this is a ray theoretical approximation). The *T(t)* component is zero (i.e., no observed tangential energy) in two cases: (1) when there is no anisotropy present and $\delta t = 0$ or (2) when the fast axis orientation is parallel or orthogonal to the direction of anisotropy and $\phi = 0°$ or 90°. These cases are deemed "null measurements" or "null splits" [*Silver and Chan*, 1991; *Menke and Levin*, 2003]. Therefore, energy on the *T(t)* component is suggestive of anisotropy but is not conclusive as dipping layers and velocity heterogeneities can also produce some transverse energy.

The two most commonly used methods in the seismology community to characterize shear wave splitting are the *Silver and Chan* [1991] (hereafter called SC) transverse component minimization method and the *Menke and Levin* [2003] (hereafter called ML) cross-convolution method. It should be noted the SC method is more widely used than ML and is readily available in the commonly utilized SplitLab software [*Wüstefeld et al.,* 2008]. *Walsh et al.* [2013] detail the shortcomings of the SC method as pertaining to error handling and there have been efforts [e.g., *Reiss and Rümpker*, 2017] to incorporate their findings into the original SC method.

Although the most common shear wave splitting methods (i.e., SC and ML) assume a single horizontal layer model when analyzing anisotropy, it is broadly accepted that this

simplistic model cannot always explain the true anisotropy. This is to be expected given the vastly different strain histories of the lithosphere and asthenosphere [*Silver and Chan*, 1991]. High variability in splitting parameters at a single station for events from differing back azimuths along with a considerable number of null splits are strong indicators of multilayered, dipping, or other complex anisotropy [*Silver and Savage*, 1994; *Schutt and Humphreys*, 2001]. There are many regions that have been hypothesized to have multilayered anisotropic structure [e.g., *Silver and Savage*, 1994; *Levin et al.*, 1999; *Romanowicz and Yuan*, 2012] and there have been efforts to develop methods that can accurately represent this scenario by way of inversion [e.g., *Silver and Savage*, 1994] or cross-convolution [e.g., *Menke and Levin*, 2003] among others [e.g., *Reiss and Rümpker*, 2017]. *Silver and Savage* [1994] produced the most widely used method for observing multilayered and dipping anisotropy by showing that plots of back azimuth vs. split time and vs. fast axis show a distinct $\pi/2$ back azimuthal periodicity. Producing these plots is not always trivial as comprehensive back azimuth coverage can be hard to obtain since high-quality SKS arrivals typically only arrive in the narrow distance range of approximately 80-120°. They then used this information to invert for the apparent splitting parameters. However, the multilayer case is not a unique solution and therefore one must use geologic and geodynamic intuition to constrain the best fitting earth model parameters.

1.5 The Cross-Convolution Method

The shear wave splitting methodology used in this study is rooted in the cross-convolution method by *Menke and Levin* [2003] for several key reasons. First, the ML method allows one to forgo the assumption of single-layer horizontal anisotropy and to consider more complex anisotropic scenarios (i.e., multilayered or dipping). Also, ML does not require the

assumption of a vertically incident raypath. This allows one to more readily constrain anisotropic complexity [*Menke and Levin,* 2003; *Long and Silver*, 2009].

The ML method constructs two time series, $x(t)$ and $y(t)$, that contain information from the observed seismograms and a hypothetical earth model such that:

$$x(t) = \tau_m * R, \quad \text{(Eqn. 1.5.1)}$$

$$y(t) = \rho_m * T, \quad \text{(Eqn. 1.5.2)}$$

where R and T are the observed radial and tangential seismograms, respectively, and ρ_m and τ_m are the predicted radial and tangential impulse responses, respectively, predicted by a hypothetical earth model, m, while * denotes convolution. The best-fitting earth model minimizes the misfit of

$$e(t) = x(t) - y(t) \quad \text{(Eqn. 1.5.3)}$$

by minimizing $||e(t)||^2$ with respect to the earth model, m, where $||.||$ denotes the L_2 norm. Thus, when $x(t) = y(t)$, ρ_m and τ_m are the correct earth model impulse responses. Recall, in shear wave splitting, that the anisotropic earth model (in this case denoted by m) is represented by two parameters, fast axis orientation (ϕ) and the split time (δt). ML use the aforementioned parameters to represent the predicted radial and tangential impulse responses, ρ_m and τ_m, of a normally-incident shear wave in an anisotropic layer as follows:

$$\rho_m = \rho_1 \, \delta(t) + \rho_2 \, \delta(t - \delta t) \quad \text{(Eqn. 1.5.4)}$$

$$\tau_m = \tau_1 \, \delta(t) + \tau_2 \, \delta(t - \delta t) \quad \text{(Eqn. 1.5.5)}$$

$$\rho_1 = cos^2(\phi - \theta) \quad \text{(Eqn. 1.5.6)}$$

$$\rho_2 = sin^2(\phi - \theta) \quad \text{(Eqn. 1.5.7)}$$

$$\tau_1 = -\tau_2 = cos(\phi - \theta) \; sin(\phi - \theta) \quad \text{(Eqn. 1.5.8)}$$

where δt is the split time, ϕ is the fast axis orientation, θ is back azimuth and $\delta(t)$ is the Dirac delta function at a given time, t. Although not modeled in this study, ML additionally define the predicted impulse responses for two anisotropic layers. The two-layer case expands the model space from two parameters to four parameters, a fast axis orientation and split time for each layer of anisotropy [*Menke and Levin*, 2003].

1.6 Statistical Augmentation to the Cross-Convolution Method

It has been noted that shear wave splitting measurements have long been lacking proper statistical assessment [e.g., *Walsh et al.*, 2013], which has hindered the application of formal hypothesis testing to shear wave splitting studies [*Castejón*, 2016]. The methodology presented by *Castejón* [2016] is rooted in the cross-convolution method but aims to quantify the effect of autocorrelated microseismic noise on the estimation of the best-fitting earth model, m_0, and then models errors with a proper bootstrapping approach.

The method gives proper standard errors, allows for appropriate station averaging, and provides a means for formal hypothesis testing. Additionally, the workflow of this method is enticing for two key reasons: 1) there is no waveform filtering required and 2) it requires substantially less user input than is needed by the widely-used SplitLab [*Wüstefeld et al*., 2008]. Downloaded radial and tangential seismograms are initially screened for good events and are then windowed with the XKS phase arrival centered, which can be heavily automated.

Castejón [2016] derived a formula for the spectral characteristics of the pre-event noise under the assumption of a single layer of anisotropy and vertically incident rays. She showed that if the true earth impulse response is used, this formula has the same spectral density as the cross-convolved signal,

$$\rho_m * T - \tau_m * R \qquad \text{(Eqn. 1.5.9)}$$

Thus, a grid search is performed over all plausible values of ρ_m and τ_m and the spectral densities of the two formulas are compared via the Whittle likelihood [*Whittle*, 1953; *Brockwell and Davis*, 1991], producing a grid of log-likelihoods that correspond to values of fast axis orientation and split time. Maximizing the Whittle log-likelihood yields estimates $\hat{\phi}$ and $\widehat{\delta t}$ for the fast axis orientation and split time, respectively.

The log-likelihood surface can serve as a basis for hypothesis testing and can be summed for many events to obtain robust station averages (Figure 1.5). Implicit in the station average summing are assumptions that the anisotropic model is correctly parameterized (such as the number of layers in the model is representative of the true earth), and each XKS ray samples the same anisotropy.

To assess uncertainty, the best-fitting earth model estimates, $\hat{\phi}$ and $\widehat{\delta t}$, and the observed radial and tangential signals are used to invert for an estimated source signal, $\widehat{S_k}$. For each bootstrap iteration, *b*, noise replicates are surrogated from r_k^* and t_k^*, where r^* and t^* are the independent pre-phase arrival noise sequences and k is an integer time index. The noise replicates, r_{kb}^* and t_{kb}^*, are uncorrelated with the pre-phase arrival noise or each other but share the same autocorrelation function, i.e., the replicates have randomized phase in each bootstrap realization. The radial and tangential time series, R_{kb} and T_{kb}, for each bootstrap iteration are constructed using the estimated source signal, impulse responses, and random-phase noise replicates as follows:

$$R_{kb} = \widehat{\rho_1}\,\hat{S}_k + \widehat{\rho_2}\,\hat{S}_{k-L} + r_{kb}^*, \qquad \text{(Eqn. 1.5.10)}$$

$$T_{kb} = \widehat{\tau_1}\,\hat{S}_k + \widehat{\tau_2}\,\hat{S}_{k-L} + t_{kb}^*, \qquad \text{(Eqn. 1.5.11)}$$

where *k* is an integer time index, *L* is the integer lag associated with the split time, and *b* is the bootstrap index.

Typically, 100 bootstrap iterations are completed, which has been empirically determined to be a sufficient amount to properly describe the standard error distribution [*Efron and Tibshirani*, 1991; *Sandvol and Hearn*, 1994; *Castejón*, 2016]. Utilizing the same grid search methodology outlined previously, each bootstrap iteration yields an estimate of fast axis orientation and split time, here called $\widehat{\phi_b}$ and $\widehat{dt_b}$, respectively. The standard error is simply calculated as the empirical standard deviation of the bootstrap replicates' distribution.

The source code obtained from *Castejón* [2016] was modified by the author of this study to enhance its flexibility. A complete replication of the source code used in this study is provided in *Appendices A and B*. The major modifications of the source code are as follows:

1) The original program was hard-coded for data with a single sample rate (50 Hz) and now it can process anything from 20 Hz to 100 Hz, although as sample rate increases, CPU runtime increases exponentially. Data less than 20 Hz are undesirable for shear wave splitting measurements. At less than 20 Hz, one begins to lose resolution in their split time measurement as impulse response delay times become harder to resolve.
2) A limitation of the original code was that it could only process a single event for a given station at a time, which substantially increased user input. Now it can be provided with a station-specific directory of XKS events (i.e., radial and transverse seismograms for each event) and the output is a summed log-likelihood, and therefore a robust station average with appropriate standard errors.
3) The code was additionally optimized to loop over a list of stations so that one can now essentially automate the entire process after the initial SKS downloading, screening and quality control.

4) Some functions (i.e., the Whittle likelihood function) were optimized to decrease CPU time.
5) Due to grid search artifacts created by the discrete integer lags, smoothing splines were used in the split time dimension to smooth the likelihood surfaces for better bootstrapping behavior.

The shear wave splitting methodology of *Castejón* [2016] was not altered and thus follows the same mathematical procedure outlined in this section. The aforementioned changes were done solely for optimization of CPU time and to remove redundant user inputs.

1.7 Figures

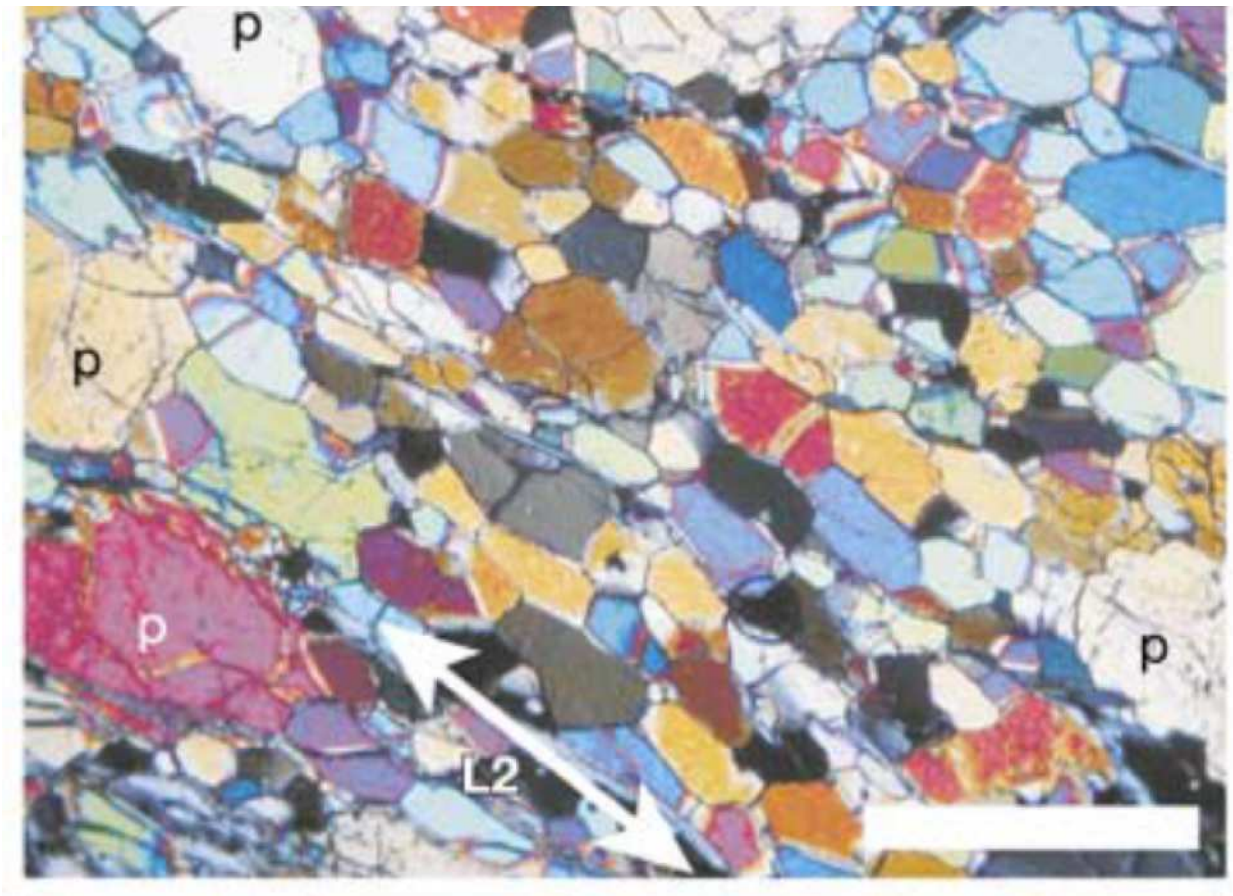

Figure 1.1: Thin-section view of olivine LPO texture in a porphyroclastic dunite under cross-polarized light. Olivine porphyroclasts (p) are surrounded by smaller neoblasts of olivine. This particular dunite comes from the Higashi-akaishi peridotite body of southwest Japan. Note how the grains have a preferred orientation in the direction of the labeled L2 lineation. The white scale-bar in the lower right is 1 mm. Figure after *Mizukami et al.* [2004].

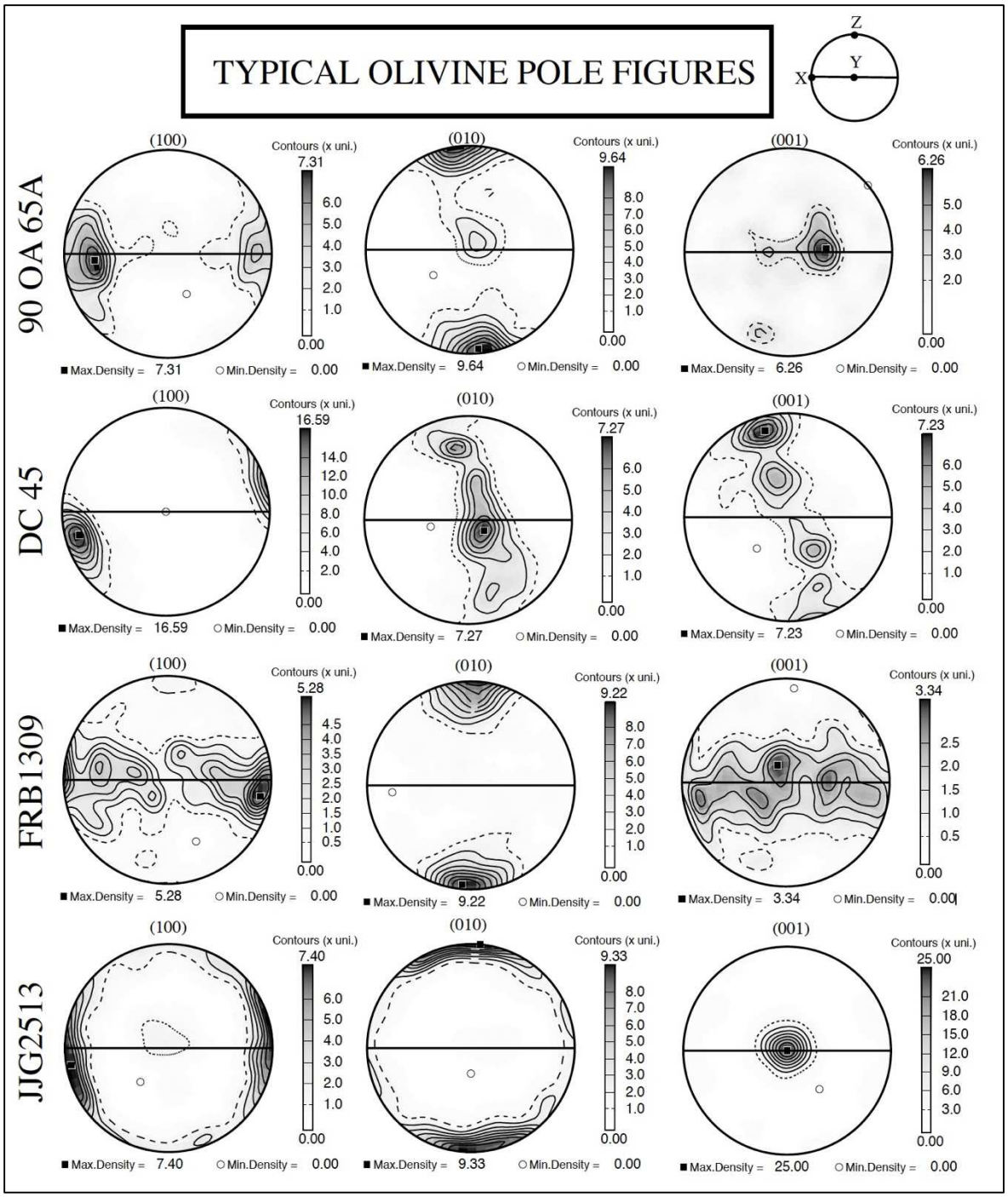

Figure 1.2: Four samples of olivine pole figures for the Miller indices (100; a-axis), (010; b-axis) and (001; c-axis). In the case of olivine, the a-axis is the fast direction of anisotropy. The contours represent the distribution of the crystal plane normals (poles) and thus represent the crystallographic texture. In this case, the horizontal line in each pole figure is the trace of the foliation plane. Figure after *Mainprice et al.* [2000].

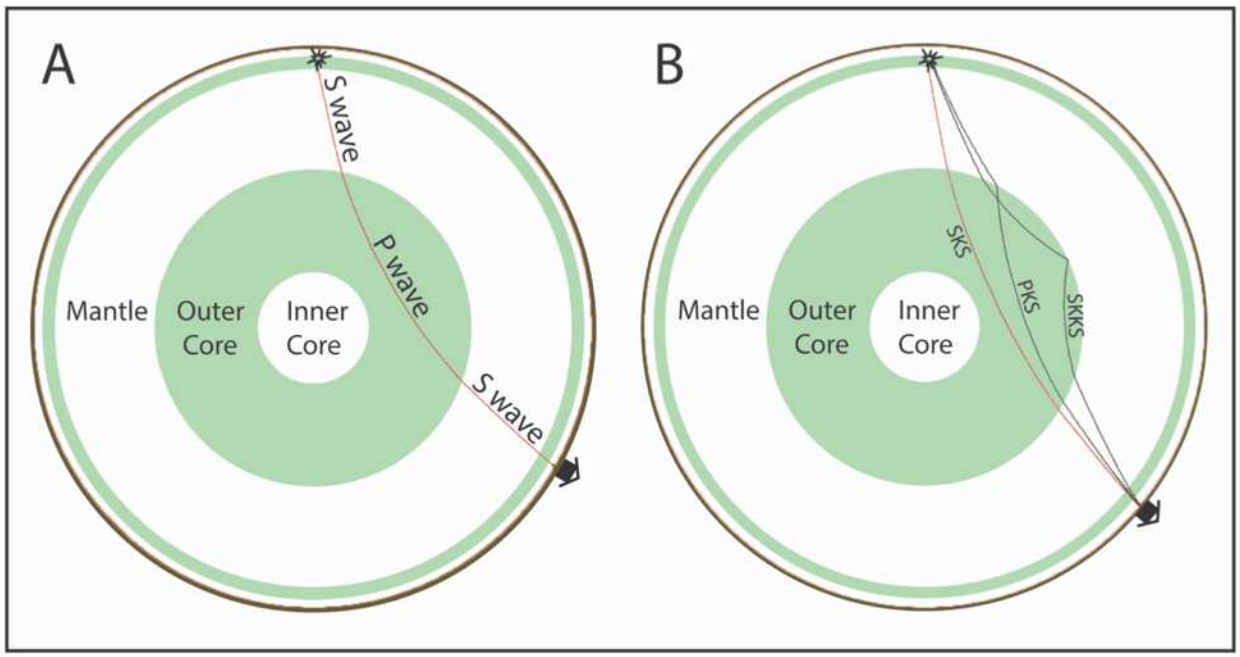

Figure 1.3: A) Cross-sectional view of an SKS ray's path through Earth's interior. In seismology parlance, the K denotes the conversion to a compressional (P) wave in the liquid outer core since shear waves cannot propagate in liquids. The conversion from P back to S on the receiver side causes the radial polarization that is ideal for shear wave splitting studies. B) Additional phases, PKS and SKKS, are shown in comparison to the SKS phase. Note that the PKS and SKKS take slightly different paths through the lower mantle but still sample the upper mantle similarly. Figure after *Crotwell et al.* [1999].

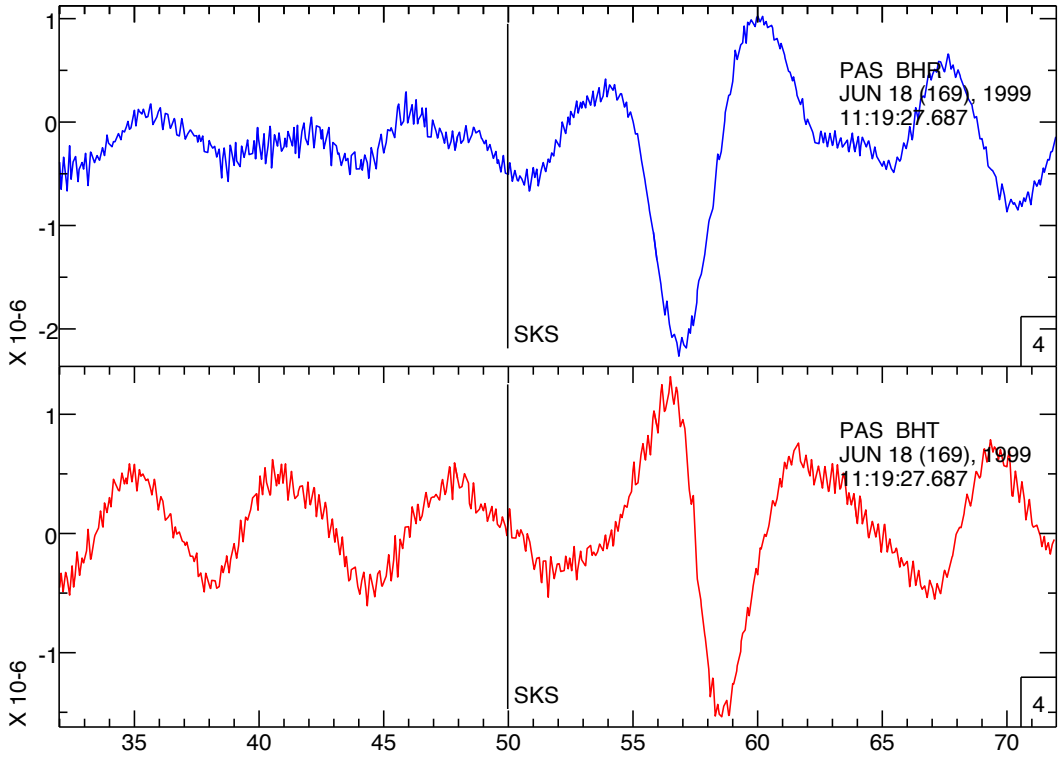

Figure 1.4: Broadband radial (blue) and transverse (red) seismograms showing a distinct SKS arrival. Note the long and short period noise in the pre-SKS arrival section of the seismogram. A benefit of using the *Castejón* [2016] method is that pre-analysis filtering is unnecessary. These seismograms are from the PAS seismic station in Pasadena, CA for an event that occurred on June 18th, 1999. Figure was created using Seismic Analysis Code (SAC) [*Goldstein et al.,* 1993; *Goldstein and Snoke*, 2005].

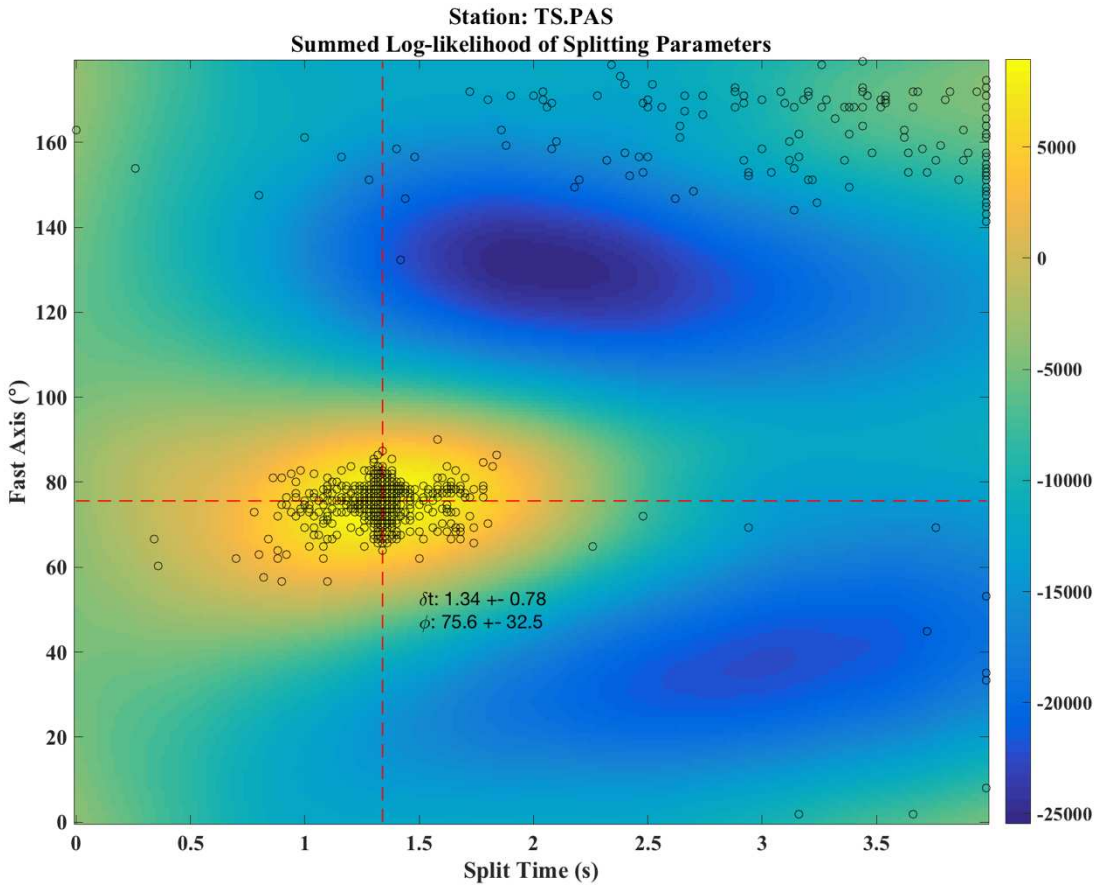

Figure 1.5: Log-likelihood surface produced using the *Castejón* [2016] shear wave splitting method for the PAS seismic station (Pasadena, CA) showing the maximum likelihood estimate (dashed lines). Each cell represents the relative statistical likelihood of a split time and fast axis pair. This surface was produced by summing the log-likelihood surfaces for 10 separate events to produce a station average. The black circles represent bootstrapping realizations, which the standard errors are calculated from. The results produced by this method are consistent with other researchers who have worked with the PAS station and surrounding area [e.g. *Liu et al.*, 1995b; *Polet and Kanamori*, 2002].

REFERENCES

Ashby, M. F., and R. A. Verrall (1973), Diffusion-accommodated flow and superplasticity, *Acta Metallurgica.*, 21(2), 149-163.

Bormann, P., P. T. Burghardt, L. I. Makeyeva, and L. P. Vinnik (1993), Teleseismic shear-wave splitting and deformations in Central Europe, *Phys. of the Earth and Planet. Interiors*, 78(3–4), 157–166.

Castejón, A. C. (2016), A new method to test shear wave splitting: improving statistical assessment of splitting parameters, *Unpublished M. Sci. Thesis*, Colorado State University, Fort Collins, CO.

Christensen, D. H., and G. A. Abers (2010), Seismic anisotropy under central Alaska from SKS splitting observations, *J. of Geophys. Res.*, 115(B4), 1–12.

Crampin, S. (1984), Effective anisotropic elastic constants for wave propagation through cracked solids, *Geophys. J. of the Royal Astronomical Soc.*, 76(1), 135–145.

Crotwell, H. P., T. J. Owens, and J. Ritsema (1999), The TauP Toolkit: Flexible Seismic Traveltime and Ray-path Utilities, *Seis. Res. Lett.,* 70(2), 154-160.

Di Leo, J. F., A. M. Walker, Z. H. Li, J. Wookey, N. M. Ribe, J. M. Kendall, and A. Tommasi (2014), Development of texture and seismic anisotropy during the onset of subduction, *Geochemistry, Geophys., Geosystems*, 15(1), 192–212.

Efron, B., and R. Tibshirani (1991), Statistical Data Analysis in the Computer Age, *Sci. New Ser.,* 253(5018), 390–395.

Frost, D. J. (2008), The upper mantle and transition zone, *Elements*, *4*(3), 171-176.

Goldstein, P., and J. A. Snoke (2005), SAC Availability for the IRIS Community, *Inc. Res. Inst. Seismol. Newsl.*, 7, 6.

Goldstein, P., D. Dodge, M. Firpo, L. Minner, and J. A. Snoke (1993), SAC2000: Signal Processing and Analysis Tools for Seismologists and Engineers, *Data Manag. Cent. Electron. Newslett.,* 8(1), 1–7.

Hanna, J., and M. D. Long (2012), SKS splitting beneath Alaska: Regional variability and implications for subduction processes at a slab edge, *Tectonophysics*, 530–531, 272-285.

Hess, H. H. (1964), Seismic Anisotropy of the Uppermost Mantle under Oceans, *Nature*, 203, 629–631.

Kaminski, É., N. M. Ribe, and J. T. Browaeys (2004), D-Rex, a program for calculation of seismic anisotropy due to crystal lattice prefferred orientation in the convective upper mantle, *Geophys. J. Int.,* 158(2), 744–752.

Karato, S. I., C. Dupas-Bruzek, and D. C. Rubie (1998), Plastic deformation of silicate spinel under the transition-zone conditions of the Earth's mantle, *Nature*, 395, 266–269.

Karato, S., H. Jung, I. Katayama, and P. Skemer (2008), Geodynamic Significance of Seismic Anisotropy of the Upper Mantle: New Insights from Laboratory Studies, *Annu. Rev. Earth Planet. Sci.*, 36(1), 59–95.

Kendall, J. M., and P. G. Silver (1996), Constraints from seismic anisotropy on the nature of the lowermost mantle, *Nature*, 381, 409-412.

Levin, V., W. Menke, and J. Park (1999), Shear wave splitting in the Appalachians and the Urals: A case for multilayered anisotropy, *J. of Geophys. Res.*, 104(B8), 17975–17993.

Liu, H., P. M. Davis, and S. Gao (1995), SKS splitting beneath southern California, *Geophys. Res. Lett.*, 22(7), 767.

Long, M. D., and E. A. Wirth (2013), Mantle flow in subduction systems: The mantle wedge flow field and implications for wedge processes, *J. Geophys. Res. Solid Earth*, 118(2), 583–606.

Long, M. D., and T. W. Becker (2010), Mantle dynamics and seismic anisotropy, *Earth Planet. Sci. Lett.*, 297(3–4), 341–354.

Long, M. D., and P. G. Silver (2009), Shear wave splitting and mantle anisotropy: Measurements, interpretations, and new directions, *Surv. in Geophys*., 30(4–5), 407–461.

Mainprice, D., G. Barrulo, and W. Ben Ismaïl (2000), The seismic anisotropy of the earth's mantle: From single crystal to polycrystal, *Geophys. Monograph*, 117, 237–264.

Mckenzie, D. P. (1979), Finite deformation during fluid flow, *Geophys. J. of the Royal Astronomical Soc.*, 58(3), 689-715.

Menke, W., and V. Levin (2003), The cross-convolution method for interpreting SKS splitting observations, with application to one and two-layer anisotropic earth models, *Geophys. J. Int.*, 154(2), 379–392.

Mizukami, T., S. R. Wallis, and J. Yamamoto (2004), Natural examples of olivine lattice preferred orientation patterns with a flow-normal a-axis maximum, *Nature*, 427(6973), 432–436.

Morelli, A., A. M. Dziewonski, and J. H. Woodhouse (1986), Anisotropy of the inner core inferred from PKIKP travel times, *Geophys. Res. Lett.,* 13(13), 1545–1548.

Nicolas, A., and N. I. Christensen (1987), Formation of anisotropy in upper mantle peridotites – a review, *Am. Geophys. Union*, 16, 111–123.

Polet, J., and H. Kanamori (2002), Anisootropy beneath Califiornia: shear wave plitting measurements using dense broadband array, *Geophys. J. Int.,* 149, 313–327.

Reiss, C., and G. Rümpker (2017), SplitRacer: MATLAB Code and GUI for Semiautomated Analysis and Interpretation of Teleseismic Shear-Wave Splitting, *Seis. Res. Lett.,* 88(2A).

Romanowicz, B., and H. Yuan, (2012), On the interpretation of SKS splitting measurements in the presence of several layers of anisotropy, *Geophys. J. Int.,* 188(3), 1129–1140.

Sandvol, E., and T. Hearn (1994), Bootstrapping shear-wave splitting errors, *Bull. Seismol. Soc. Am.,* 84(6), 1971–1977.

Schutt, D. L., and E. D. Humphreys (2001), Evidence for a deep asthenosphere beneath North America from western United States SKS splits, *Geology*, 29(4), 291–294.

Silver, P. G., and W. W. Chan (1991), Shear Wave Splitting and Sub continental Mantle Deformation, *J. Geophys. Res*., 96, 429–454.

Silver, P. G. (1996), Seismic anisotropy beneath the continents: Probing the depths of geology, *Annu. Rev. Earth Planet. Sci.*, 24(1), 385–432.

Silver, P. G., and M. K. Savage (1994), The interpretation of shear-wave splitting parameters in the presence of two anisotropic layers, *Geophys. J. Int.*, 119(3), 949–963.

Stein, S., and M. Wysession (2003), An introduction to seismology, earthquakes, and earth structure, *Blackwell Publ*., Oxford, UK, ISBN:0-86542-078-5.

Turner, F. (1942), Determination of extinction angles in monoclinic pyroxenes and amphiboles, *Am. J. of Sci.*, 240(8), 571.

Verma, R. (1960), Elasticity of some high-density crystals, *J. Geophys. Res*., 65(2), 757.

Walsh, E., R. Arnold, and M. K. Savage (2013), Silver and Chan revisited, *J. Geophys. Res. Solid Earth*, 118(10), 5500–5515.

Wüstefeld, A., G. Bokelmann, C. Zaroli, and G. Barruol (2008), SplitLab: A shear-wave splitting environment in Matlab, *Computers and Geosci.*, 34(5), 515–528.

Zhang, S., and S. Karato (1995), Lattice preferred orientation of olivine aggregates deformed in simple shear, *Nature*, 375, 774-777.

CHAPTER 2

2.1 Introduction

The northern Canadian Cordillera (NCC) is a wide amalgamation of Phanerozoic mountain belts and plateaus that extend from the Yukon-British Columbia border to the Beaufort Sea. It is geographically bounded by the North American craton to the east and Alaska to the west. Present day deformation in the region is driven primarily by ongoing (since ~10Ma) impingement of the Yakutat Indentor (YT), a small oceanic-continental terrane that migrated northwestward alongside the Pacific plate (PA) until it collided obliquely with the North American plate (NA) in the Gulf of Alaska [e.g., *Bruns*, 1983; *Hyndman et al.,* 2005]. The oblique collision of the YT has resulted in crustal thickening, uplift of the coastal Saint Elias and Chugach Mountains, and intense seismicity therein (Figure 2.1). A small amount of convergence (~1-5 mm/year) is transferred inland, across the Denali and Tintina fault systems, to the Mackenzie Mountains (MM) and Richardson Mountains (RM) [*Hyndman et al.,* 2005; *Maréchal et al.,* 2015]. These ranges are actively uplifting, despite being many hundreds of kilometers from the plate margin.

The MM are an arcuate fold and thrust belt that extend approximately 1000 km into the interior of northern North America. Unlike much of the NCC, the MM are presently seismically active. Thrust earthquakes in the MM and limited geodetic measurements suggest that the area between the Denali Fault and MM is presently converging to the northeast relative to the North American craton [*Mazzoti and Hyndman*, 2002; *Leonard et al.*, 2007]. Further to the north, the RM show predominantly strike slip faulting mechanisms, consistent with northeast-directed motion [*Leonard et al.,* 2007].

The deep inboard uplift of the MM may provide insights into the orogenic processes that have driven other mountain building events far from the plate boundary, such as the Laramide Orogeny in the U.S. *Mazzotti and Hyndman* [2002] have suggested an orogenic float hypothesis to the MM, in which motion from the YT is transferred over a lower crustal detachment layer in the lower crust, causing the MM to pile up on the edge of the Canadian Craton. This hypothesis presumes a weak and thin lithosphere such that the mantle plays little role in the uplift. Alternatively, modeled asthenospheric tractions show evidence of convergence under the Mackenzie Mountains, which may produce contraction and uplift [*Finzel et al.,* 2015]. These mechanisms may produce distinct mantle fabrics observed through shear wave splitting, the topic of this study.

The central section of the NCC is marked by two large right-lateral faults, the Tintina and the Denali. These are not very active currently, except for some slow motion on the Denali fault [e.g., *Eberhart-Phillips et al.,* 2003], but each slipped approximately 400 km during the early Cenozoic, a period of transpressional tectonics [*Rasendra et al.,* 2014]. This sheared region lies over a hypothesized slab window, where recent volcanism may be associated with dry asthenospheric upwelling [*Thorkelson et al,* 2011]. The lithosphere here is associated with various Paleozoic and Mesozoic autochthonous terranes sometimes called the Intermontaine Terranes--assembled in a transpressional environment [e.g., *Colpron et al.,* 2015]. West of the Denali fault lies the Insular Terranes, which are a set of accreted terranes of oceanic affinity [e.g., *Colpron et al.*, 2015]. Roughly in the south of the MM and region of study (Figure 2.1), the Liard Transfer zone (LTZ) is the inferred westward extension of an asymmetric rifted margin of Laurentia [e.g., *Audet et al.,* 2016].

Current neotectonic activity is taking place over a complex geologic framework, and measurements of crustal and mantle fabric alignments through seismic anisotropy observations show a similar complexity of structures, but that can be broadly characterized into five subregions. The Canadian craton to the east of the Cordilleran Deformation Front has strong crustal radial anisotropy [*Dalton and Gaherty*, 2013]. Shear wave splitting measurements show mantle fabric aligned close to absolute plate motion (APM) [*Courtier et al.,* 2010; *Audet et al*., 2016; *DeMets et al.,* 2010]. Within the Cordillera, but south of the LTZ, shear wave splitting also indicates mantle aligned close to APM [*Audet et al*., 2016]. North of the LTZ, shear wave splitting fast orientations are aligned in the direction of the Denali and Tintina faults. Receiver function studies find significant amounts of crustal and lithospheric mantle anisotropy, which roughly align with the Tintina and Denali faults, but are not very coherent [*Tarayoun et al.,* 2017; *Rasendra et al.,* 2014]. Due to sparse historical station coverage within and around the MM, there have been no observations as to how these anisotropy trends change in the MM between the Tintina fault and the front of cordilleran deformation.

Here we present new SKS wave splitting measurements in the NCC and east-southeast Alaska for > 150 stations. These include recently deployed Transportable Array (TA) and MM stations, along with nearly all past regional broadband stations for which data is available. A new technique to calculate station averages and characterize parameter uncertainty is applied as part of the analysis [*Castejón,* 2016]. Teleseismic shear wave splitting observations offer our most direct constraint on the strain history of the lithosphere and asthenosphere [e.g., *Silver and Chan,* 1991; *Silver,* 1996]. In complex tectonic settings, such as the MM and NCC, one should expect both lithospheric and asthenospheric contributions to measured splitting parameters since these layers have experienced different strain histories. Multiple layers of anisotropy can be queried by

looking at periodicity in plots of back-azimuth vs. fast axis [e.g., *Silver and Savage*, 1994], by performing inversions of single-layer parameters [e.g., *Reiss and Rümpker*; 2017], or by using the cross-convolution two-layer functional forms [*Menke and Levin,* 2003].

2.2 Data and Methods

Shear wave splitting is analogous to optical birefringence and occurs when a seismic shear wave encounters an anisotropic medium (such as an aligned olivine fabric in the mantle). Upon encountering the medium, the shear wave is split into two orthogonally polarized waves travelling at different velocities, with the faster wave typically following the dominant direction of anisotropy and the slower, orthogonal wave, lagging behind [e.g., *Silver and Chan,* 1991; *Silver*, 1996; *Long and Becker*, 2010]. Two parameters typically used to quantify anisotropy from shear wave splitting are called the fast axis orientation (ϕ) and the split time (δt), which refer to the polarization direction of the faster wave and the time lag between the two split shear waves, respectively. Core-refracted phases (i.e., SKS, SKKS, and PKS) are particularly useful since they are radially polarized upon leaving the outer core, which isolates the observed anisotropy to the receiver side of the ray path.

For the current study, SKS phases were requested from the IRIS Data Management Center and the Canadian National Data Center for stations spanning a latitude range of 58°-70° N and a longitude range of 110°-145° W using generally accepted event search criteria [e.g., *Liu and Gao*, 2013], including an epicentral distance range of 80-125° and $M_w >= 5.8$. Of particular note is that our dataset includes recently-deployed Yukon Territory TA stations and an approximately 550-mile-long transect of tightly-spaced broadband instruments that were deployed through the MM during the summer of 2016. Overall, data for 154 stations were collected and 700 waveform pairs were manually screened and accepted as high-quality core-

refracted shear waves. There was an average of 5 events per station, with a range of 1-24 events and an overall total of 137 events (Figure 2.2).

For the analysis, we chose to use a new method by *Castejón* [2016] for calculating splitting parameters and their resulting uncertainties. This method is based on the cross-convolution method [*Menke and Levin,* 2003] but yields better statistical characterization of splitting parameters by quantifying the effect of microseismic noise on the estimation of ϕ and δt. Correlation structures of the noise are accounted for to create a log-likelihood surface of the splitting parameters that provides the statistical context for formal hypothesis testing of anisotropy. The method calculates log-likelihood grid search surfaces for every station-event pair and then sums them to get formal station averages, if the assumption of a single-layer of anisotropy is correct. A benefit to this method is that it works with noisy data that does not need to be bandpass filtered or have a particularly high signal-to-noise ratio. Thus, the only preprocessing that needs to be done is the rotation to radial and transverse coordinates and initial waveform screening and windowing. For consistency in our analysis, we chose to recalculate all the regional stations' splitting parameters, rather than compile them from past regional studies [e.g., *Courtier et al.,* 2010; *Rasendra et al.*, 2014; *Audet et al*., 2016].

2.3 Results and Regional Trends

The station-averaged shear wave splitting results are summarized in Figure 2.3 and Table 2.1 and can be broken down into five subregions discussed in the introduction: (1) the PA-NA subduction zone/YT collisional zone; (2) the Denali and Tintina transpressional fault systems and the region bounded by them; (3) the area near the BC-YK border along the Tintina fault; (4) the Canadian shield and northeastern Alaska passive margin; and (5) the transitional inboard region between (2) and (4) that includes the MM and central-eastern Alaska. Fast axis

orientations within the PA-NA collisional margin are complex. They are predominately oriented about N10°E, but a significant minority have a nearly perpendicular orientation that coincides with the orientation of the Denali fault. There are a wide range of split times, and many were at the the grid search maximum δt value of 3.98 seconds. Between the Denali and Tintina faults fast axes are parallel to subparallel with fault strikes but show some variety in split times. This is not the case along the southern Tintina fault (e.g., around the BC-YK border) where fast axes are oriented east-west and do not follow the strike of the Tintina. Generally, the stations within the Canadian shield show uniform southwest-northeast fast axes and split times of around 1 s, although we see some erratic behavior on the margins of this region (i.e., along the MM-shield margin). Fast axes along the MM transect (blue dots in Figure 2.3A) parallel the Tintina fault in the southwest and then gradually rotate about 50° to a near APM orientation at Great Bear Lake on the Slave craton. A similar transition is shown moving from central to northeastern Alaska as fault-parallel fast axes transition to east-west orientations before further rotation to a more southwest-northeast orientation.

Back azimuth vs. fast axis plots are shown for two example stations where splitting parameters vary substantially between events, even ones from similar back azimuths (Figure 2.4; stations are green dots on Figure 2.3). SKS waveforms at these stations are noticeably noisy and measurements may suffer from crustal reverberations.

2.4 Discussion

In the PA-NA subduction zone/YT collisional zone, the back azimuthal heterogeneity in splitting parameters may be explained by a variety of factors: namely, complex mantle flow around the subducting slab [e.g. *Long and Silver*, 2008] and within the slab window [e.g. *Thorkelson et al,* 2011] dipping, frozen anisotropy in the subducting slab, and heterogeneous

anisotropic structure in the deformed lithosphere. Notably, significant but not strongly coherent crustal anisotropy also seems to exist here [*Rasendra et al.,* 2014]. The very large split times (i.e., greater than 2.5 s) that are oriented slightly clockwise from north (nearly normal to Pacific APM) could be due to hydrated mantle that exhibits B-type olivine deformation and serpentenization [e.g., *Jung and* Karato, 2001; *Jung et al.,* 2006; Long *and Wirth*, 2013], although the strong back azimuth-dependence of fast axis orientations suggests either rays from different directions are sampling different anisotropy, or anisotropic structures are more complex than a single layer. Abrupt fast axis rotations around the 70-km slab contour have been noted in central Alaska, and the current set of observations may have a similar cause [e.g., *Christensen and Abers*, 2010]. Further analysis of this region will require the ability to model more complex structures, as the current station averaging method is predicated upon a single-layer of anisotropy.

Along and between the dextral Denali and Tintina faults, the overwhelmingly fault-parallel to subparallel fast axis directions agree well with past studies that show similar crustal anisotropy, consistent with lithospheric shearing [e.g., *Courtier et al.,* 2010, *Rasendra et al.,* 2014; *Audet et al.,* 2016] and possible transpressional accretion of exotic terranes [e.g., *Johnston*, 2001]. While it is likely that NA plate motion is responsible for some component of asthenospheric flow-related fabric beneath the plate [e.g., *Marone and Romanowicz,* 2007; *Courtier et al.,* 2010], lithospheric mantle-penetrating shear zones can induce strong enough anisotropy (4%-11%; *Audet et al.,* 2016) [e.g., *Vauchez et al.,* 2012; *Zietlow et al.,* 2014] to produce significant anisotropic delay times. No clear indication of back azimuthal variation in splitting parameters is observed within this subregion, which may indicate that asthenospheric

fabrics are disorganized, perhaps from asthenospheric upwelling associated with a slab window [*Thorkelson et al.,* 2011].

A change in mantle properties occurs south of the Liard transfer zone, where fast axes rotate from fault parallel to a more east-west orientation. *Audet et al.* [2016] suggest the lithosphere here has a different fabric, and *Courtier et al.* [2010] have conjectured that the lithospheric fabric is weaker here such that the east-west direction represents a stronger component of asthenospheric anisotropy in the observed splitting. In either case, the LTZ seems to delineate a lithospheric fabric boundary. Notably the east-west fast axes end at the Teslin fault, suggesting this is the western extent of the LTZ.

Seismic anisotropy in the Canadian shield is well-studied [e.g., *Vinnik et al.,* 1992; *Silver,* 1996; *Snyder and Bruneton*, 2007; *Courtier et al.,* 2010; *Audet et al.*, 2016] and is predominantly ascribed to asthenospheric flow, although lithospheric complexities are noted [*Snyder and Bruneton*, 2007]. In the current study, cratonic splits and those within northeastern Alaska match these previous studies; however, a few unusual sites should be noted. The station at Inuvik, NWT, Canada (orange dot on Fig. 2.2A), lies on thick sediment and has crustal reverberations observed on the SKS waveforms. These forms of signal-generated noise are not accounted for in the *Castejón* [2016] method, which assumes noise is stationary. In the presence of reverberations, null splitting measurements are favored, because there is no good model of anisotropy that fits the data. Individual splitting measurements can have spurious splitting times, including very large values of δt such as are found along the coast ranges, and station averages will tend to produce likelihood plots that sum these multiple null-like measurements, which constructively reinforce only for near-zero split times. Consequently, the station-averaged split time tends to be small. Station WGLY (red dot on Fig. 2.2A) also exhibits anomalous behavior,

with a very large splitting time of δt = 3.16 +/- 0.96 s, and a fast axis orientation near APM. Here, *Audet et al.* [2016] find a fast axis orientation parallel to the deformation front, and nearly orthogonal to the current finding. This heterogeneity seems to support the notion that WGLY could be a near-null station that is very sensitive to microseismic noise.

The data from the recently deployed MM station transect present an opportunity to examine mantle fabrics in this hitherto uninstrumented region, and assess mechanisms for MM uplift. If the orogenic float hypothesis is a primary mechanism, then crustal deformation will be decoupled from that in the mantle [e.g., *Oldow et al.,* 1990; *Mazzoti and Hyndman*, 2002; *Hyndman et al.,* 2005]. Alternatively, if mantle tractions are driving uplift, these should produce a distinct pattern of splitting consistent with predicted traction directions [e.g., *Finzel et al.,* 2015]. These processes can be complementary if the lower crust is not fully decoupled from the mantle [*Finzel et al.,* 2015]. Since fast axis directions in the MM approximately follow the predicted traction field put forth by *Finzel et al*. [2015], tractions could play a role in MM uplift, although the source of this asthenospheric flow is uncertain. The splits from southwest to northeast across the MM may then indicate a gradual transition from anisotropic fabric generated by the lithospheric mantle-penetrating shearing to asthenosphere-dominated anisotropy, perhaps the signature of traction-inducing flows (Figure 2.5). Given the parautochthonous nature of most of the region east of the Tintina (except for the Yukon-Tanana terrane) [*Colpron et al*., 2015], it might be expected that lithospheric anisotropy in the MM is not as dominated by transpression as the terranes to the west, and lithospheric shear associated with dextral faulting on the Tintina will diminish in magnitude as one moves to the northeast, producing the observed rotation towards asthenosphere-dominated splitting. As noted by other studies, the correlation between crustal and lithospheric mantle anisotropy in the Tintina-Denali region indicates that the crust and

lithospheric mantle were not fully decoupled at the time of shearing [*Tarayoun et al.,* 2017; *Rasendra et al.,* 2014]; however, it is likely that most shearing took place before the ~10Ma beginning of the Yakutat convergence [e.g., *Bruns*, 1983; *Hyndman et al.,* 2005], so this observation does not rule out an orogenic float component to the MM uplift. It is remarkable that lithospheric anisotropy seems to dominate the shear wave splitting in most of the NCC, given that large scale tomography models [e.g., *Schaeffer and Lebedev,* 2014] find low velocities in the mantle west of the MM, presumably indicating thin lithosphere. This would be consistent with the asthenosphere below the Tintina-Denali subregion having limited development of anisotropic fabric due to recent upwelling from the opening of the slab window. However, given the similarity between predicted traction directions and APM in the region of the MM transect, our conclusion must remain equivocal until ongoing complimentary studies on lithospheric structures in this region are completed.

2.5 Conclusion

Measurements of shear wave splitting using a new methodology show five distinct regions of strain. The plate margin shows complex anisotropy; eastward, between the Denali and Tintina faults, anisotropy aligns with the dominant northwest-southeast direction of shear associated with the ~1000 km of right-lateral offset in the region; we conclude the lithosphere in the region is highly sheared along with the crust, but the asthenosphere has minimal coherent anisotropy. The Mackenzie Mountains are a transitional region, where lithospheric anisotropy gives way to asthenosphere-dominated anisotropy as one moves to the northeast. Fast axis directions rotate towards APM, but never quite reach it, and are consistent with predicted lithospheric basal tractions [*Finzel et al.,* 2015]. Recent MM uplift is probably associated with both plate margin forces from the Yakutat Indenter [*Mazotti and Hyndman*, 2002] and with

asthenospheric flow applying tractions on the lithosphere [*Finzel et al.,* 2015]. The relative contribution of each remains obscure. Anisotropy in the Slave craton and in northeast Alaska is mostly consistent with APM. South of the Liard transfer zone, we also find a rotation in fast axes consistent with the lithospheric fabric change as proposed by *Audet et al.* [2016].

2.6 Figures

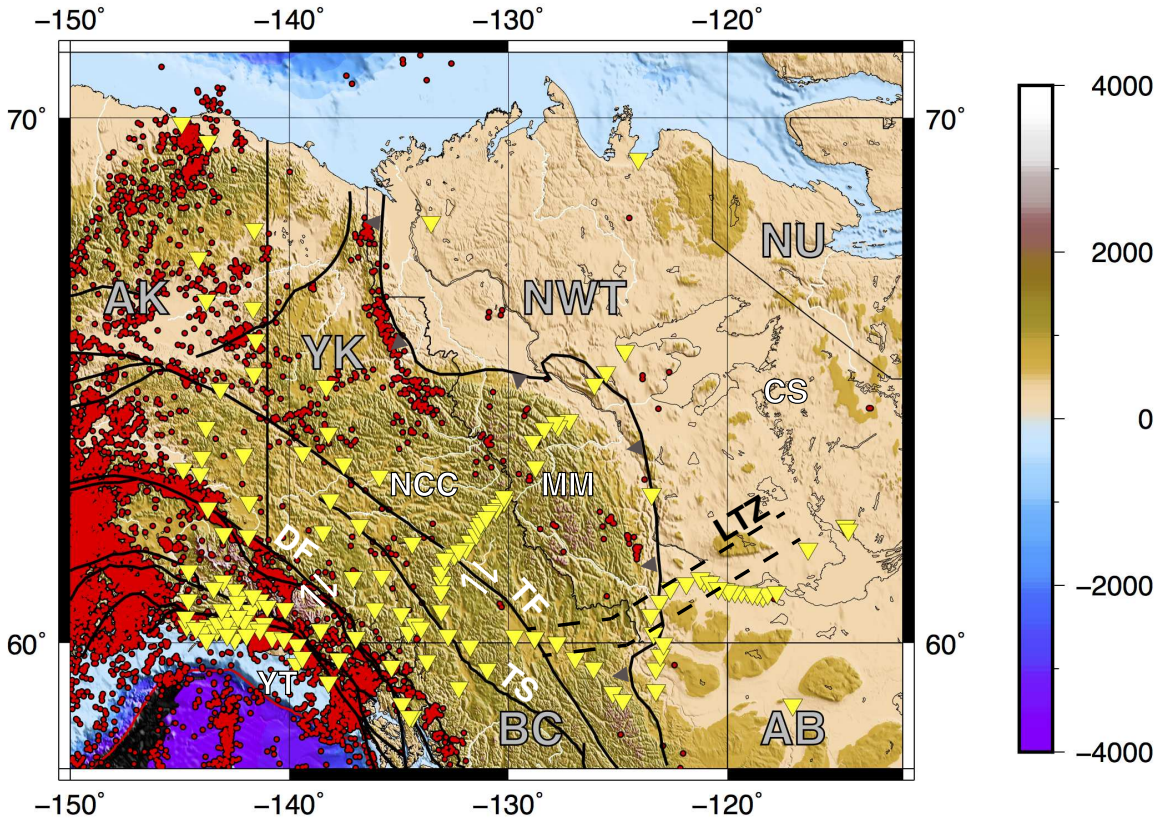

Figure 2.1: Map depicting the study area for this experiment. Seismic events ($M_w > 2$) since the year 2000 are shown as red dots and broadband seismometers used for this study are shown as yellow triangles. The tectonic boundaries labeled are: DF-Denali Fault, TF-Tintina Fault, TS-Teslin Fault, LTZ-Liard Transfer Zone, and the line with the saw tooth pattern is the inferred limit of cordilleran deformation. The provinces and states labeled are: AB-Alberta; AK-Alaska; BC-British Columbia; NWT-Northwest Territories; NU-Nunavut; YK-Yukon. The geologic provinces labeled are: NCC-Northern Canadian Cordillera, MM-Mackenzie Mountains; YT-Yakutat Block, and CS-Canadian Shield.

Figure 2.2: Map showing the seismic event distribution (red circles) used for this study. The center of the study area is denoted by the star and the black lines illustrate the back azimuths from the study area to the events.

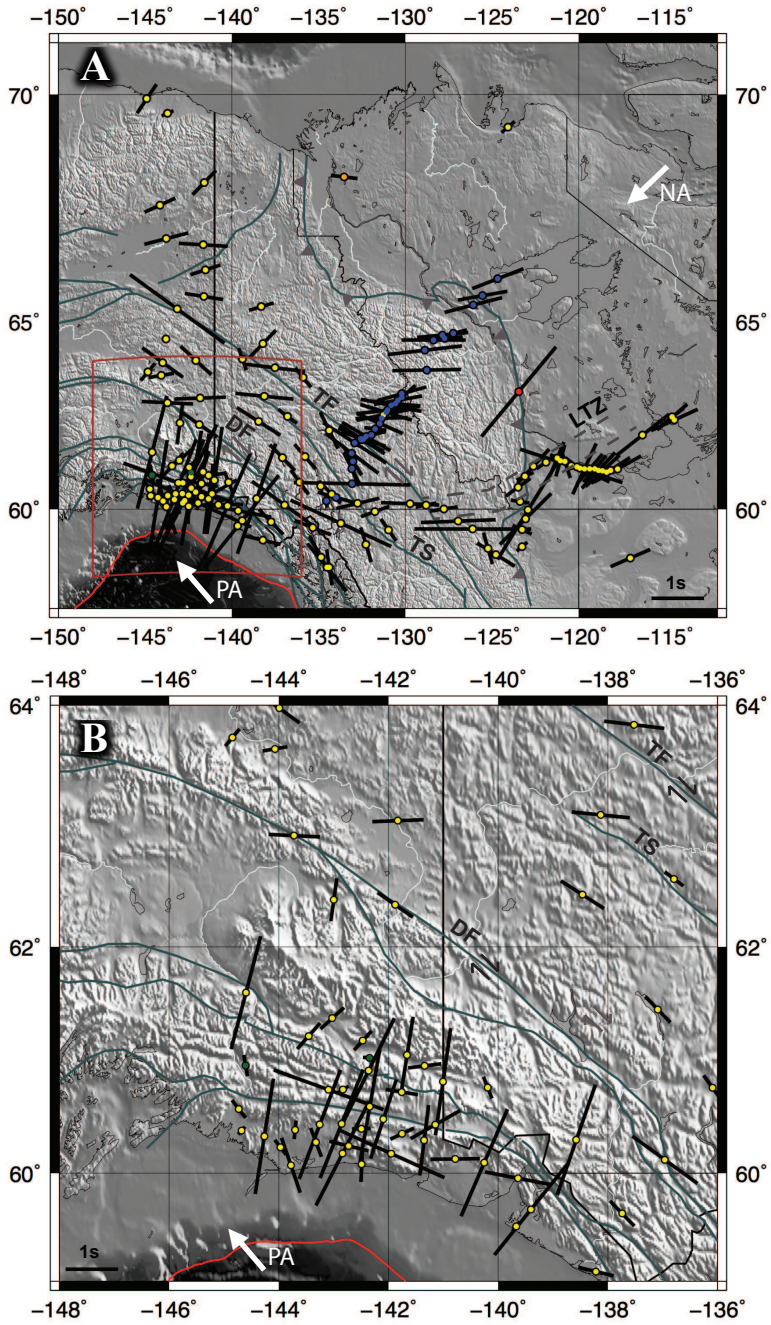

Figure 2.3: A) Station-averaged teleseismic shear wave splitting results are shown as black lines, where the azimuth of the line is the fast axis orientation and the length of the line is proportional to the accumulated split time (scale bar shows 1 s length). The gray lines denote tectonic boundaries and/or faults; DF-Denali fault, TF-Tintina Fault, TS-Teslin Fault, and the easternmost line with the saw tooth pattern is the inferred limit of cordilleran deformation. The Pacific (PA) and North America (NA) absolute plate motions (APM) are shown as white arrows and are calculated from *DeMets et al.* [2010]. B) Inset map of southeastern Alaska showing a dense subset of stations within the PA-NA subduction zone and the Yakutat block collisional zone. For display purposes, all measurements with $\delta t > 2.5$ s were set to a maximum length proportional to 2.5 s.

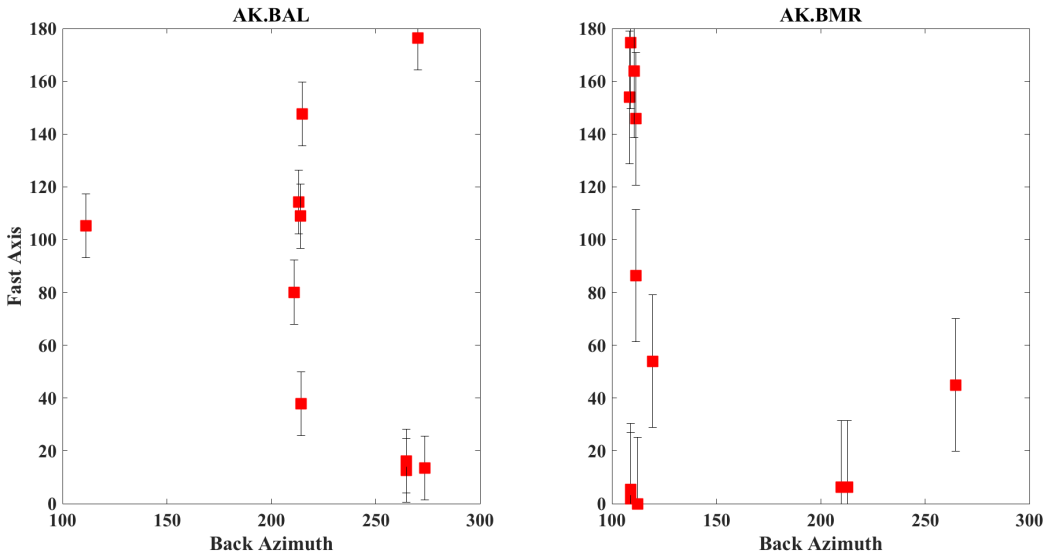

Figure 2.4: Back azimuth vs. fast axis plots for two stations (AK.BAL and AK.BMR; green dots on Figure 2.2) within the Alaska subduction/Yakutat block collisional zone. Error bars represent the 1-σ standard error bounds. Note the different fast axis measurements despite events arriving from similar back azimuths.

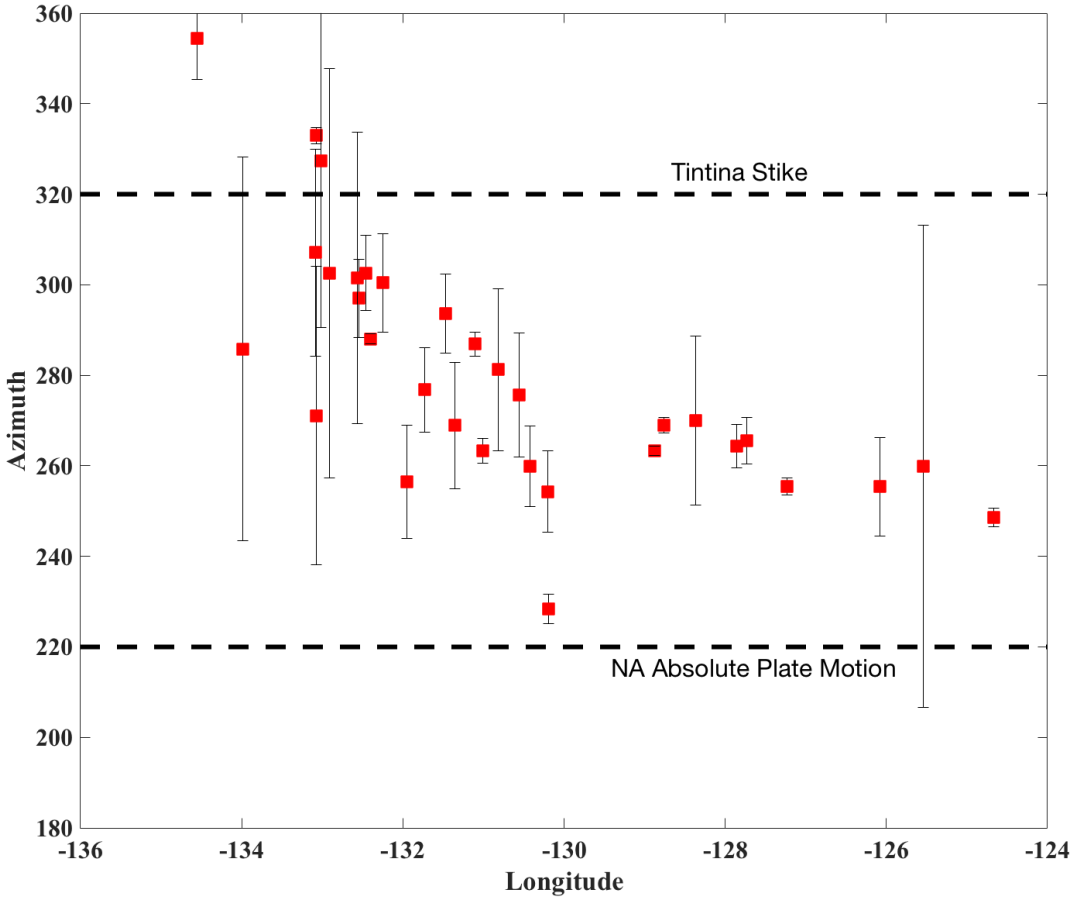

Figure 2.5: Fast axes at MM-network stations (blue dots in figure 2.1A) plotted vs. longitude to illustrate the transition from Tintina fault-parallel fast axes to near North American (NA) plate motion-parallel fast axes. Error bars represent the 1-σ standard error.

2.7 Tables

Table 2.1: Station averaged shear wave splitting results from bootstrapped summed likelihoods. The maximum grid search values for δt and ϕ were 3.98 s and 180°, respectively.

Station	Lon (°)	Lat (°)	δt (s)	ϕ (°)	$\sigma_{\delta t}$	σ_{ϕ}
A02	-123.2644	59.4036	0.45	114.8	0.04	11.5
A03	-123.0624	59.72	1.55	45.0	0.11	13.0
A04	-122.9164	59.9811	3.45	31.5	0.79	22.2
A05	-123.3726	60.2191	0.40	99.0	1.35	29.0
A06	-123.4932	60.6312	0.65	54.0	0.09	38.8
A07	-123.0947	60.9368	0.40	65.3	0.06	2.6
A08	-122.6145	61.2215	1.00	42.8	0.10	26.7
A09	-121.8821	61.3318	0.50	56.3	1.86	52.5
A10	-121.2366	61.4451	0.75	22.5	0.40	31.0
A12	-119.9317	61.1654	1.40	114.8	0.85	8.2
A13	-119.0696	61.1446	0.75	40.5	0.36	25.6
A14	-118.3811	61.0522	0.80	58.5	1.35	23.8
A17	-116.3181	62.0765	1.45	51.8	1.40	48.1
B01	-123.2676	58.8985	0.30	49.5	0.22	47.8
B03	-124.7726	58.6614	0.95	121.5	0.41	39.4
B04	-125.2314	58.8471	0.70	164.3	1.15	23.8
B06	-126.1088	59.4223	3.30	90.0	0.29	4.4
B07	-126.9501	59.6548	1.60	87.8	1.64	60.3
B08	-127.7758	60.0057	0.60	81.0	1.02	14.1
B09	-128.8046	60.1197	0.45	78.8	0.03	10.7
B10	-129.72	60.1576	1.25	92.3	0.12	8.7
B12	-131.7444	59.933	0.65	69.8	0.28	6.6
B13	-132.7457	60.1694	0.95	76.5	0.85	40.4
B15	-134.2474	60.434	0.55	135.0	0.24	17.3
BAGL	-142.0915	60.4896	1.78	18.0	0.25	22.4
BAL	-142.3462	61.036	0.28	93.6	0.91	12.3
BARK	-142.4931	60.403	0.40	88.2	0.04	86.9
BARN	-141.6622	61.0595	1.66	9.0	1.51	55.7
BC01	-121.0621	61.3736	0.70	15.8	0.91	9.8
BC02	-120.7937	61.3537	0.75	162.0	0.08	9.3
BC03	-120.423	61.2296	2.30	108.0	0.40	7.7

Station	Lon (°)	Lat (°)	δt (s)	ϕ (°)	$\sigma_{\delta t}$	σ_{ϕ}
BC04	-120.0994	61.2038	0.65	128.3	0.38	47.3
BC05	-119.6663	61.1475	1.20	24.8	0.01	7.2
BC06	-119.3666	61.1437	0.85	40.5	0.77	16.2
BC07	-118.8572	61.1041	1.05	42.8	0.75	3.4
BC08	-118.6296	61.0899	1.00	47.3	0.10	9.1
BC09	-118.1597	61.1046	1.00	56.3	0.45	40.3
BC10	-117.7584	61.1411	1.15	60.8	0.22	10.7
BCP	-139.6369	59.9534	1.44	100.8	0.14	8.4
BERG	-143.7004	60.3932	0.40	6.3	0.03	9.0
BESE	-134.8559	58.5792	1.04	151.2	0.88	55.8
BMR	-144.6051	60.9677	0.46	170.1	1.18	25.1
C26K	-144.9122	69.9175	0.75	33.8	0.29	19.9
C27K	-143.7114	69.626	0.28	65.3	0.38	63.1
C36M	-124.0703	69.3475	0.38	49.5	1.60	35.4
CRQ	-143.0926	60.7523	3.98	109.8	0.25	11.2
CTG	-141.3401	60.9649	0.72	82.8	0.42	16.5
CYK	-142.4872	60.0823	0.76	2.7	0.76	28.2
DAWY	-139.3909	64.0655	0.50	160.9	0.47	34.7
DCPH	-138.2154	59.0906	0.78	103.5	0.75	45.3
DOT	-144.0697	63.6482	0.54	80.1	0.85	30.1
E27K	-141.5951	68.1861	0.73	43.9	0.13	19.1
F26K	-144.1455	67.6946	0.73	65.3	0.08	3.9
G26K	-143.7848	66.9498	0.98	75.4	0.10	2.2
G27K	-141.6549	66.8088	1.05	93.4	0.12	8.8
GOAT	-144.7292	60.5805	0.48	142.2	0.05	2.0
GRIN	-143.321	60.2805	0.66	159.3	0.49	82.3
GRNC	-141.7558	60.7315	0.70	99.0	1.00	39.5
H27K	-141.5265	66.2305	0.68	72.0	0.08	9.2
HILA	-117.0203	58.5561	0.93	66.4	1.03	28.6
HMT	-144.2623	60.3351	3.96	9.0	0.50	11.2
I26K	-143.1541	65.3064	3.63	126.0	0.76	32.4
I27K	-141.6153	65.6035	0.83	99.0	0.42	1.4
I29M	-138.3063	65.3609	0.55	73.1	0.52	19.1
INK	-133.5254	68.3065	0.58	96.8	0.16	25.5
ISLE	-142.3406	60.6024	3.98	9.9	0.36	9.2

Station	Lon (°)	Lat (°)	δt (s)	ϕ (°)	$\sigma_{\delta t}$	σ_{ϕ}
J26K	-143.799	64.5654	0.13	95.6	1.12	2.8
J29M	-138.2158	64.453	0.80	43.9	0.37	27.9
JIS	-134.3848	58.2758	0.78	171.9	1.45	31.9
K27K	-142.0758	64.0292	0.90	132.8	0.11	5.2
K29M	-137.5201	63.8433	1.30	96.8	0.43	21.4
KHIT	-143.251	60.4427	2.80	20.7	1.86	16.4
KIAG	-142.3605	60.9231	3.28	26.1	0.14	12.5
KULT	-142.7234	60.2474	0.86	103.5	1.69	18.4
L27K	-141.8275	63.0618	1.10	87.8	0.17	8.8
L29M	-138.129	63.109	1.25	95.6	0.13	8.7
LOGN	-141.0048	60.824	2.32	8.1	0.51	26.5
M26K	-142.9963	62.4013	0.93	7.9	0.95	57.4
M27K	-141.878	62.3579	0.93	124.9	0.34	9.7
M29M	-138.4624	62.4435	1.10	122.6	1.33	43.5
M30M	-136.7935	62.5763	0.50	127.1	0.50	9.7
M31M	-134.3906	62.2024	0.88	154.1	0.56	19.6
MAYO	-135.8921	63.5958	0.54	141.3	1.23	36.6
MCAR	-143.024	61.3836	0.68	47.7	0.33	9.1
MENT	-143.7194	62.938	1.10	92.7	0.13	8.4
MM04	-134.5509	60.24	0.30	174.4	0.02	9.0
MM05	-133.9864	60.3412	0.83	105.8	1.58	42.4
MM07	-133.0706	60.7272	2.68	91.1	0.24	33.0
MM08	-133.079	61.1496	0.78	153.0	1.43	1.8
MM09	-133.021	61.3568	0.70	147.4	0.06	36.8
MM10	-133.0888	61.5783	1.43	127.1	0.53	22.8
MM11	-132.9148	61.8625	1.60	122.6	0.58	45.2
MM12	-132.542	61.9516	1.10	117.0	0.12	8.7
MM13	-132.4607	61.9525	1.13	122.6	0.43	8.3
MM14	-132.4057	61.9684	1.00	108.0	0.18	1.1
MM15	-132.5664	61.9727	1.08	121.5	0.56	32.2
MM16	-132.2521	62.0379	1.20	120.4	0.11	10.9
MM17	-131.9483	62.079	0.63	76.5	0.01	12.5
MM18	-131.734	62.2425	0.48	96.8	0.24	9.3
MM19	-131.471	62.3867	1.08	113.6	0.89	8.7
MM20	-131.3592	62.5318	1.13	88.9	0.27	13.9

Station	Lon (°)	Lat (°)	δt (s)	ϕ (°)	$\sigma_{\delta t}$	σ_{ϕ}
MM21	-131.1072	62.6859	1.15	106.9	0.87	2.7
MM22	-131.0116	62.7442	1.35	83.3	0.16	2.8
MM23	-130.8161	62.8713	1.33	101.3	0.46	17.9
MM24	-130.5583	62.9183	1.08	95.6	1.01	13.7
MM25	-130.4189	63.005	1.05	79.9	0.40	8.9
MM26	-130.1928	63.081	0.78	48.4	0.01	3.3
MM27	-130.2005	63.1751	1.08	74.3	0.05	9.0
MM29	-128.765	63.7858	1.48	88.9	0.41	1.7
MM30	-128.8747	64.289	1.60	83.3	0.16	1.0
MM32	-128.371	64.5422	1.38	90.0	0.56	18.7
MM33	-127.7333	64.5833	0.78	85.5	0.21	5.1
MM34	-127.8557	64.6683	1.10	84.4	0.20	4.8
MM35	-127.2313	64.7075	0.60	75.4	0.09	1.9
MM38	-126.0753	65.4007	1.28	75.4	0.63	10.9
MM39	-125.5394	65.6227	1.08	79.9	0.92	53.3
MM40	-124.6708	66.0246	1.18	68.6	0.36	2.1
MMPY	-131.2625	62.6189	1.18	78.3	0.10	6.0
N25K	-144.5982	61.6061	3.78	14.6	0.07	9.0
N30M	-137.0885	61.4593	0.78	136.1	0.51	46.5
N31M	-135.7796	61.4862	0.70	139.5	0.74	59.5
N32M	-133.0818	61.1512	0.80	158.6	0.21	13.9
NICH	-143.9692	60.2361	0.40	143.1	1.18	30.2
O28M	-140.1906	60.7718	0.50	158.6	0.63	48.4
O29M	-138.5755	60.3024	3.98	19.1	0.40	9.3
O30N	-136.0906	60.7704	0.65	144.0	0.41	29.1
P29M	-137.7381	59.6304	0.75	136.1	0.61	44.9
P30M	-136.9598	60.1218	1.73	126.0	1.63	46.3
P32M	-133.7147	59.5898	2.38	114.8	0.13	1.3
PIN	-140.2525	60.0959	3.36	23.4	0.18	5.0
PNL	-139.4014	59.667	3.98	38.7	0.13	1.4
PTPK	-142.4672	61.1871	0.56	42.3	0.20	14.1
Q32M	-132.2691	58.9601	0.78	163.1	0.08	11.9
R32K	-134.5181	58.2747	1.33	140.6	1.27	45.3
R33M	-130.9673	59.3946	0.58	145.1	0.57	52.7
RAG	-144.6773	60.3863	0.22	42.3	1.66	24.8

Station	Lon (°)	Lat (°)	δt (s)	ϕ (°)	$\sigma_{\delta t}$	σ_{ϕ}
RIDG	-144.8462	63.7399	0.48	39.6	0.56	64.0
RKAV	-141.3478	60.2994	1.52	7.2	0.09	9.5
SAMH	-140.7828	60.1294	1.06	89.1	0.95	40.7
SCRK	-143.9905	63.9761	1.08	126.0	0.94	19.2
SKAG	-135.329	59.4601	0.84	111.6	1.83	21.1
SSP	-142.8388	60.1791	3.98	27.0	0.74	21.6
SUCK	-143.779	60.072	1.24	161.1	0.35	84.0
TABL	-141.1443	60.4399	1.22	60.3	0.22	12.0
TGL	-142.8292	60.7541	0.28	59.4	0.59	38.3
VRDI	-143.4545	61.2275	0.74	41.4	0.53	33.7
WAX	-142.8529	60.448	3.64	21.6	0.03	8.5
WGLY	-123.4584	63.2281	3.16	39.6	0.96	23.5
WHY	-134.8806	60.6597	0.25	168.8	0.61	21.8
WTLY	-128.7961	60.1133	0.08	102.6	0.22	18.5
YAH	-141.751	60.3583	0.56	64.8	0.20	2.6
YKAW1	-114.4842	62.4822	1.10	65.3	1.04	56.3
YKAW3	-114.6099	62.5616	0.63	52.9	0.59	35.0
YKW3	-114.6099	62.5616	0.85	49.5	0.09	1.3

REFERENCES

Audet, P., C. Sole, and A. J. Schaeffer (2016), Control of lithospheric inheritance on neotectonic activity in northwestern Canada?, *Geology*, 44(10), 807–810.

Bruns, T.R. (1983), Model of origin of the Yakutat block, and accreting terrane in the northern Gulf of Alaska, *Geology*, 11, 718–721.

Castejón, A. C. (2016), A new method to test shear wave splitting: improving statistical assessment of splitting parameters, *Unpublished M. Sci. Thesis*, Colorado State University, Fort Collins, CO.

Christensen, D. H., and G. A. Abers (2010), Seismic anisotropy under central Alaska from SKS splitting observations, *J. Geophys. Res.*, *115*(B4), 1–12.

Colpron, M., J. L. Crowley, G. Gehrels, D. G. F. Long, D. C. Murphy, L. Beranek, and L. Bickerton (2015), Birth of the northern Cordilleran orogen, as recorded by detrital zircons in Jurassic synorogenic strata and regional exhumation in Yukon, *Lithosphere*, 5, 541–562.

Courtier, A.M., J. B. Gaherty, J. Revenaugh, M. G. Bostock, and E. J. Garnero (2010), Seismic anisotropy associated with continental lithosphere accretion beneath the CANOE array, northwestern Canada, *Geology*, 38, 887–890.

Dalton, C. A., and J. B. Gaherty (2017), Seismic anisotropy in the continental crust of northwestern Canada, *Geophys. J. Int*. 2013, 193, 338–348.

DeMets, C., R. G. Gordon, and D. F. Argus (2010), Geologically current plate motions, *Geophys. J. Int*., 181(1), 1–80.

Eberhart-Phillips, D., P.J. Haeussler, J.T. Freymueller, et al. (2003), The 2002 Denali fault earthquake, Alaska: a large magnitude, slip-partitioned event, *Science*, 300, 1113–1118.

Finzel, E.S., L.M. Flesch, K.D. Ridgway, W.E. Holt, and A. Ghosh (2015), Surface motions and intra-plate continental deformation in Alaska driven by mantle flow, *Geophys. Res. Lett*., 42, 4350–4358.

Hyndman, R. D., P. Flück, S. Mazzotti, T. J. Lewis, J. Ristau, and L. Leonard (2005), Current tectonics of the northern Canadian Cordillera, *Canadian J. of Earth Sci.,* 42(6), 1117–1136.

Johnston, S.T. (2001), The Great Alaskan Terrane Wreck: reconciliation of paleomagnetic and geological data in the northern Cordillera, *Earth Planet. Sci. Lett.,* 193, 259-272.

Jung, H., I. Katayama, Z. Jiang, T. Hiraga, and S. Karato (2006), Effect of water and stress on the lattice-preferred orientation of olivine, *Tectonophys*., 421, 1–22.

Jung, H. (2011), Seismic anisotropy produced by serpentine in mantle wedge, *Earth Planet. Sci. Lett.,* 307, 535–543.

Leonard, L. J., R. D. Hyndman, L. Nykolaishen, M. Schmidt, and S. Hippchen (2007), Current deformation in the northern Canadian Cordillera inferred from GPS measurements, *J. Geophys. Res.,* 112, 1–15.

Liu, K. H., and S. S. Gao (2013), Making reliable shear-wave splitting measurements, *Seis. Soc. of Am. Bull.,* 103(5), 2680–2693.

Long, M. D., and P. G. Silver (2008), The subduction zone flow field from seismic anisotropy: A global view, *Science*, 319, 315–318.

Long, M. D., and T. W. Becker (2010), Mantle dynamics and seismic anisotropy, *Earth Planet. Sci. Lett.*, *297*(3–4), 341–354.

Long, M. D., and E. A. Wirth (2013), Mantle flow in subduction systems: The mantle wedge flow field and implications for wedge processes, *J. Geophys. Res. Solid Earth*, 118(2), 583–606.

Maréchal, A., S. Mazzotti, J.L. Elliott, J.T. Freymueller, and M. Schmidt (2015), Indentor-corner tectonics in the Yakutat–St. Elias collision constrained by GPS, *J. Geophys. Res.,* 120, 3897–3908.

Marone, F., and B. Romanowicz (2007), The depth distribution of azimuthal anisotropy in the continental upper mantle, *Nature*, 447, 198– 201.

Mazzotti, S., and R.D. Hyndman (2002), Yakutat collision and strain transfer across the northern Canadian Cordillera, *Geology*, 30, 495–498.

Menke, W., and V. Levin (2003), The cross-convolution method for interpreting SKS splitting observations, with application to one and two-layer anisotropic earth models, *Geophys. J. Int.*, *154*(2), 379–392.

Oldow, J.S., A.W. Bally, and H.G. Ave Lallemant (1990), Transpression, orogenic float, and lithospheric balance, Geology, 18, 991–994.

Rasendra, N., M. Bonnin, S. Mazzotti, and C. Tiberi (2014), Crustal and upper-mantle anisotropy related to fossilized transpression fabric along the Denali fault, northern Canadian Cordillera, *Seis. Soc. of Am. Bull.,* 104, 1964–1975.

Reiss, C., and G. Rümpker (2017), SplitRacer: MATLAB Code and GUI for Semiautomated Analysis and Interpretation of Teleseismic Shear-Wave Splitting, *Seis. Res. Lett.,* 88(2A).

Schaeffer, A. J., and S. Lebedev (2014), Imaging the North American continent using waveform inversion of global and USArray data, *Earth Planet. Sci. Lett.,* 402, 26-41.

Silver, P. G., and W. W. Chan (1991), Shear Wave Splitting and Sub continental Mantle Deformation, *J. Geophys. Res*., 96, 429–454.

Silver, P. G., and M. K. Savage (1994), The interpretation of shear-wave splitting parameters in the presence of two anisotropic layers, *Geophys. J. Int.*, *119*(3), 949–963.

Silver, P. G. (1996), Seismic anisotropy beneath the continents: Probing the depths of geology, *Annu. Rev. Earth Planet. Sci.*, *2*4(1), 385–432.

Snyder, D., and M. Bruneton (2007), Seismic anisotropy of the Slave craton, NW Canada, from joint interpretation of SKS and Rayleigh waves, *Geophys. J. Int.*, 169(1), 170–188.

Tarayoun, A., P. Audet, S. Mazzotti, and A. Ashoori (2017), Architecture of the crust and uppermost mantle in the northern Canadian Cordillera from receiver functions, *J. Geophys. Res. Solid Earth*, 122, 5268–5287.

Thorkelson, D. J., J. K. Madsen, and C. L. Sluggett (2011), Mantle flow through the Northern Cordilleran slab window revealed by volcanic geochemistry, *Geology*, 39(3), 267–270.

Vauchez, A., A. Tommasi, and D. Mainprice (2012), Faults (shear zones) in the Earth's mantle, *Tectonophys.,* 558–559, 1–27.

Vinnik, L. P., L. I. Makeyeva, A. Milev, and Y. Usenko (1992), Global patterns of azimuthal anisotropy and deformation in the continental mantle, *Geophys. J. Int.,* 111, 433–447.

Zietlow, D.W., A.F. Sheehan, P.H. Molnar, M.K. Savage, G. Hirth, J.A. Collins, and B.H. Hager (2014), Upper mantle seismic anisotropy at a strike-slip boundary: South Island, New Zealand, *J. Geophys. Res.,* 119, 1020– 1040.

CHAPTER 3

3.1 Future Work

The northern North American Cordillera is ripe for further investigation with the onset of available Transportable Array (TA) data in Alaska and Yukon Territory (Figure 3.1). This thesis can serve as an initial study of the anisotropy in the Mackenzie Mountains and surrounding area. With more data availability and community focus in this area, expanding on these findings will be crucial to our understanding of the region. Recommendations for future work are thus outlined in this section.

As the Mackenzie Mountains transect and TA data become more widely available over the coming years, scientists will be well-positioned to solve many complex tectonic problems in the region. The denser coverage will result in better constrained shear wave splitting measurements and thus a better understanding of the anisotropy in the region. Another intriguing future study is to combine the shear wave splitting results in a joint inversion with surface wave tomography to tightly constrain both azimuthal and radial anisotropy in the Mackenzie Mountains and the northern North American Cordillera in general. These studies will lead to years of collaboration with Canadian colleagues and will furthermore lay the ground work for potential large-scale projects in the future.

Although assuming a single horizontal layer of anisotropy is a common place to start in shear wave splitting studies, one makes significant assumptions about the orientation and symmetry of anisotropy, while also simplifying the XKS ray paths as being vertically incident. Given the variability of the shear wave splitting measurements in this area, we can say with relative confidence that these assumptions do not hold uniformly in the study region. It is

plausible, in this complex tectonic region, that there is both a lithospheric and asthenospheric component to the true anisotropy [e.g., *Courtier et al.,* 2010; *Rasendra et al.*, 2014; *Audet et al*., 2016]. Therefore, a natural recommendation for future work is to expand the cross-convolution method (ML) [*Menke and Levin*, 2003] to these more complex anisotropy scenarios. The impulse response functions are easily adaptable to dipping- and/or two-layer situations although the problem becomes increasingly ill-posed because of the long period of XKS phases and the need for data from multiple directions and/or angles of incidence.

Using the predicted XKS ray angle of incidence would also be useful, especially in constraining potentially dipping anisotropy. With sufficient data, one could theoretically query non-core-refracted phases to glean information about anisotropy on the source-side or along the total ray path of S waves, for example, by treating the source-side and receiver-side anisotropy with the same approach as 2 or more layers of receiver-side anisotropy. The ML impulse responses can be modified via a functional fit that combines the incoming angle of the S-wave with the dip of the anisotropic layer.

3.2 Obtaining Seismic Data from the IRIS DMC and CNSN

This section outlines the data retrieval procedures that were used to obtain seismic data for this study. The data used herein can be obtained via Standing Order for Data (SOD) [*Owens et al.*, 2004]. SOD is a useful and widely-used software package that provides a command line front-end to the Incorporated Research Institutions for Seismology (IRIS) Data Management Center (DMC). SOD allows one to write XML "recipes" that contain information about the events, stations, and seismograms that one would like to request. The SOD recipe used to obtain XKS phases for this study is presented in *Appendix C*. It has been optimized for shear wave splitting studies and can thus be used by future graduate students or researchers. In short, these

XML files request events in the proper epicentral distance ranges, rotate seismograms to radial and tangential components, remove the data mean, remove the data trend, and calculate the signal-to-noise ratio. They also have the availability to remove overlapping phases that may interfere with good XKS arrivals. Thus, SOD is a very valuable tool for requesting seismic data, especially for shear wave splitting studies where considerable data screening is needed before any analysis can begin.

The remaining Canadian data that cannot be obtained from SOD are retrieved using an Automated Data Retrieval Procedure (AutoDRM). The data that are obtained from the Canadian National Seismic Network (CNSN) is much more involved than a SOD request. Although no CNSN data was used herein, one large contribution of this study was the development of a procedure for obtaining this difficult-to-get data. The AutoDRM procedure is well-documented on the CNSN website (http://www.earthquakescanada.nrcan.gc.ca/stndon/AutoDRM/). In order to format an AutoDRM request properly, one must create a text file table that has information about the stations, events, and time windows that are to be requested. To do this properly and efficiently, a shell script can be written that compiles all the above mentioned criterion. In this shell script, SOD is used to find events and then phase arrivals are calculated using TauP [*Crotwell et al.*, 1999]. The user then sends this information in a formatted email to autodrm@seismo.nrcan.gc.ca and if the data exists, a response is returned with the proper link to download the requested data. This method of downloading data is not ideal for users requesting very large datasets and often fails on very large requests, such as the one that was necessary for this study. Our research group found a workaround by contacting colleagues directly at the CNSN. They allowed us to send them a table containing all the above mentioned information directly and then pulled the large data request from their database. A secure File Transfer

Protocol (FTP) was then established by which we could download the data. An example CNSN data request table is provided in *Appendix D* and will be a significant head start for future students and researchers working with CNSN data. Scripts created by the author of this study to compile these requests are located in the Schutt research group directory, /data/seismo/.

3.3 Data Screening and Processing for Shear Wave Splitting Analysis

The *Castejón* [2016] method of shear wave splitting requires seismograms that are centered on the XKS arrival with equal amounts of pre-arrival and SKS-arrival time samples. As mentioned in Chapter 1, the seismograms do not need to be filtered or tapered for the analysis. The data are ready for analysis when they have been screened, trimmed, and organized into station directories. We suggest the following procedure to prepare data for analysis:

1) Download events for each seismic station that is to be included in the study and organize them into station-specific directories that include radial and transverse seismograms for each event. Note that the SOD recipe used for this study rotates seismograms into radial and transverse components upon download.
2) Use TauP or SOD to identify the arrival time of XKS phases. Once should also remove overlapping phases.
3) Screen individual events for clear XKS arrivals (Figure 3.2) using Seismic Analysis Code (SAC) [*Goldstein et al.*, 2003]. This can be done relatively quickly using a shell script that calls the function "ppk" in a SAC macro.
4) Center and trim seismograms so that there are 20 seconds of pre-arrival noise and 20 seconds of SKS-signal for a total length of 40 seconds. This task can also be automated with a SAC macro.

5) Create lists of events for each station and name them "<station>_events.txt". The shear wave splitting code uses these files to know which seismograms to process.
6) Create a text file list of stations that are to be processed. This must match the station's name in step 5).

The CNSN data requires a few initial steps that the data from the IRIS DMC does not. The seismograms come in miniseed format and are organized by event rather than station. Additionally, they do not include any station or event metadata (i.e., latitude, longitude, magnitude, etc.). The IRIS DMC provides tools, such as "rdseed", for conversion from miniseed to SAC but much of the process requires some form of shell scripting for maximum efficiency. To prepare the CNSN data for the procedure above, we suggest the following steps:

1) Using rdseed, convert the miniseed files to SAC format by merging the raw miniseed files with the dataless file that contains station metadata.
2) Write a shell script that that pulls the event metadata from your initial list of events that were sent to the CNSN for data retrieval. This should invoke a SAC macro that sets the appropriate event headers for the desired metadata (i.e., depth, magnitude, latitude, longitude, etc.).
3) Re-organize the seismograms into station directories that include radial and transverse seismograms for each event.
4) Rotate seismograms to radial and transverse coordinates.
5) From here begin at step 2) in the previous procedure to complete the data processing.

The shell scripts and SAC macros used in this body of work can be used by future graduate students and researchers to speed up data processing time. All scripts, SAC macros, and other coding done for this project are located in the Schutt research group directory, /data/seismo/.

3.4 Using the *Castejón* [2016] Shear Wave Splitting Code

As mentioned in Chapter 1.6, modifications were made to the source code of *Castejón* [2016] to increase the efficiency of the analysis. The code is written in "R", which is an open-source programming language that has been quickly gaining popularity across different science disciplines [*R Core Team*, 2016]. The language functions much like MATLAB and has vast libraries of functions. It is required that R version 3+ is installed on the computer that is being used for the analysis. R scripts and functions can be sourced from the command line of a Macintosh or Linux computer but it is highly recommended that one uses a GUI, such as "RStudio", for debugging purposes.

The code is now setup to run an entire station worth of events at once. It consists of only two files: "Step_1_Setup.R" and "Step_2_Data.R". Once the processing steps in Chapter 3.3 are completed, the code can be run in just a few sequential steps:

1) Source Step_1_Setup.R to import all requisite functions.
2) Change the variable "pathname" (line 18) to the path of the master directory that has the station-event directories and station-event list text files.
3) Modify the variable "stations" (line 21) to query the text file list of stations to be analyzed.
4) Source Step_2_Data.R to run analysis. View outputs of log-likelihood surface, splitting parameters, and bootstrapping results.

Note that the code is parallelizable and there are additional variables at the beginning of Step_2_Data.R that allow for cluster creation and implementation.

The modified versions of Step_1_Setup.R and Step_2_Data.R obtained from *Castejón* [2016] are displayed in *Appendices A and B*.

3.5 Figures

Figure 3.1: Station map of northwestern Canada and eastern Alaska. The triangles and squares represent the current and past seismic stations in the region as of August 2017. Note the incredible station sparsity in the northeast area of this map.

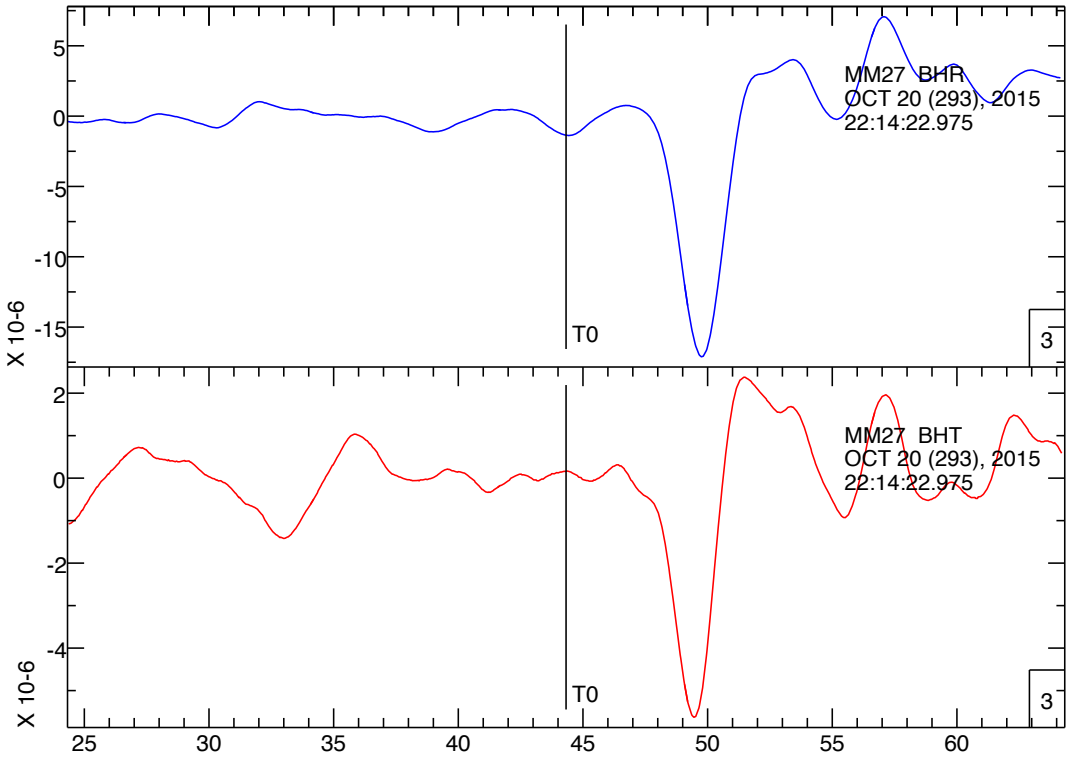

Figure 3.2: Example of clear SKS arrival on radial and transverse channels. This event was recorded at Macmillan Pass, YT, Canada, and has not been used for any shear wave splitting study prior to this one.

REFERENCES

Audet, P., C. Sole, and A. J. Schaeffer (2016), Control of lithospheric inheritance on neotectonic activity in northwestern Canada?, *Geology*, 44(10), 807–810.

Castejón, A. C. (2016), A new method to test shear wave splitting: improving statistical assessment of splitting parameters, *Unpublished M. Sci. Thesis*, Colorado State University, Fort Collins, CO.

Courtier, A.M., J. B. Gaherty, J. Revenaugh, M. G. Bostock, and E. J. Garnero (2010), Seismic anisotropy associated with continental lithosphere accretion beneath the CANOE array, northwestern Canada, *Geology*, 38, 887–890.

Crotwell, H. P., T. J. Owens, and J. Ritsema (1999), The TauP Toolkit: Flexible Seismic Traveltime and Ray-path Utilities, *Seis. Res. Lett.,* 70(2), 154-160.

Goldstein, P., D. Dodge, M. Firpo, and L. Minner (2003), SAC2000: Signal Processing and Analysis Tools for Seismologists and Engineers, *IASPEI Int. Handb. Earthq. Eng. Seis.,* 81, 1613–1620.

Menke, W., and V. Levin (2003), The cross-convolution method for interpreting SKS splitting observations, with application to one and two-layer anisotropic earth models, *Geophys. J. Int.*, 154(2), 379–392.

R Core Team (2016), R: A language and environment for statistical computing, R Foundation for Statistical Computing, Vienna, Austria, https://www.R-project.org/.

Rasendra, N., M. Bonnin, S. Mazzotti, and C. Tiberi (2014), Crustal and upper-mantle anisotropy related to fossilized transpression fabric along the Denali fault, northern Canadian Cordillera, *Seis. Soc. of Am. Bull.,* 104, 1964–1975.

APPENDICES

APPENDIX A

```
## Script to set up functions for cross-convolution shear wave splitting code
## Must run before sourcing Step_2_Data.R
## Authors: Dr. F. Jay Breidt, Ana Corbalan, and Derek Witt
## Last Edited: JAN 2017 - Derek Witt

#########################################################################
#########################################################################
#########################################################################
# Set up manually the function rsac to open and read sac files in R
rsac<- function(files, endian = .Platform$endian)
{
  if(length(endian) == 1 & length(files) > 1)
    endian <- rep(endian, length(files))
  n <- length(files)
  data <- vector(mode = "list", length = n)
  for(i in 1:n)
  {
    file <- files[i]
    zz <- file(file, "rb")
    h1 <- readBin(con = zz, what = numeric(), n = 70, size = 4,
                  endian = endian[i])
    dim(h1) <- c(5, 14)
    h1 <- aperm(h1)
    # NA values:
    h1[h1 == -12345] <- NA
    h2 <- readBin(con = zz, what = integer(), n = 35, size = 4,
                  endian = endian[i])
    dim(h2) <- c(5, 7)
    h2 <- aperm(h2)
    # NA values:
    h2[h2 == -12345] <- NA
    h3 <- readBin(con = zz, what = logical(), n = 5, size = 4,
                  endian = endian[i])
    h4 <- readBin(con = zz, what = character(), n = 1, size = 4,
                  endian = endian[i])
    # Define header variables:
    dt <- h1[1, 1]
    depmin <- h1[1, 2]
    depmax <- h1[1, 3]
    scale <- h1[1, 4]
    odelta <- h1[1, 5]
    b <- h1[2, 1]
    e <- h1[2, 2]
    o <- h1[2, 3]
    a <- h1[2, 4]
    f <- h1[5, 1]
    stla <- h1[7, 2]
    stlo <- h1[7, 3]
    stel <- h1[7, 4]
    stdp <- h1[7, 5]
    evla <- h1[8, 1]
    evlo <- h1[8, 2]
    evel <- h1[8, 3]
    evdp <- h1[8, 4]
    mag <- h1[8, 5]
    dist <- h1[11, 1]
    az <- h1[11, 2]
    baz <- h1[11, 3]
```

```
    gcarc <- h1[11, 4]
    cmpaz <- h1[12, 3]
    cmpinc <- h1[12, 4]
    nzyear <- h2[1, 1]
    nzjday <- h2[1, 2]
    nzhour <- h2[1, 3]
    nzmin <- h2[1, 4]
    nzsec <- h2[1, 5]
    nzmsec <- h2[2, 1]
    norid <- h2[2, 3]
    nevid <- h2[2, 4]
    N <- h2[2, 5]
    idep <- h2[4, 2]
    iztype <- h2[4, 3]
    leven <- h3[1]
    lpspol <- h3[2]
    kstnm <- substr(h4, 1, 8)
    kstnm <- sub("-12345", "      ", kstnm)
    kevnm <- substr(h4, 9, 24)
    kevnm <- sub("-12345", "      ", kevnm)
    khole <- substr(h4, 25, 32)
    khole <- sub("-12345", "      ", khole)
    ko <- substr(h4, 33, 40)
    ko <- sub("-12345", "      ", ko)
    ka <- substr(h4, 41, 48)
    ka <- sub("-12345", "      ", ka)
    kcmpnm <- substr(h4, 161, 168)
    kcmpnm <- sub("-12345", "      ", kcmpnm)
    knetwork <- substr(h4, 169, 176)
    knetwork <- sub("-12345", "      ", knetwork)
    kinst <- substr(h4, 185, 192)
    kinst <- sub("-12345", "      ", kinst)
    seek(con = zz, where = 632)
    x <- readBin(con = zz, what = numeric(), n = N,
                 size = 4, endian = endian[i])
    close(zz)
    data[[i]] <- list(amp = x, dt = dt, depmin = depmin, depmax = depmax,
                      scale = scale, odelta = odelta,
                      b = b, e = e, o = o, a = a, f = f,
                      stla = stla, stlo = stlo, stel = stel, stdp = stdp,
                      evla = evla, evlo = evlo, evel = evel, evdp = evdp,
                      mag = mag, dist = dist, az = az, baz = baz, gcarc = gcarc,
                      cmpaz = cmpaz, cmpinc = cmpinc,
                      nzyear = nzyear, nzjday = nzjday, nzhour = nzhour,
                      nzmin = nzmin, nzsec = nzsec,
                      nzmsec = nzmsec, norid = norid,
                      nevid = nevid, N = N,
                      units = idep, iztype = iztype,
                      leven = leven, lpspol = lpspol,
                      sta = kstnm, kevnm = kevnm, khole = khole,
                      ko = ko, ka = ka,
                      comp = kcmpnm, knetwork = knetwork, kinst = kinst)
  }
  class(data) <- "rsac"
  invisible(data)
}
## Code: Thompson, E. M. and Lees, J. M. \code{Rsac}
#########################################################################
#########################################################################
#########################################################################
preprocess<-function(R,T,sigma=-9,difference=TRUE){
            # Center the data by subtracting off the mean
            if(difference){
```

```
                R<-diff(R,1,1)
                T<-diff(T,1,1)
        }# end if difference
        R<- R-mean(R)
        T<- T-mean(T)
        if(sigma<0){
                sigma_R<-sqrt(var(R))
                sigma_T<-sqrt(var(T))
                sigma<-(sigma_R+sigma_T)/2
        }# end if negative sigma
        R<-R/sigma
        T<-T/sigma
        out<-list(R=R,T=T,sigma=sigma)
        return(out)
}
##########################################################################
##########################################################################
##########################################################################
unpreprocess<-function(R,T,Sigma=1,undifference=TRUE){
   if(undifference){
        R <- cumsum(c(0,R))
        T <- cumsum(c(0,T))
   }
   #R<- R+mean(R)
   #T<- T+mean(T)
   R <- Sigma*R
   T <- Sigma*T
   out<-list(R=R,T=T)
   return(out)
}
##########################################################################
##########################################################################
##########################################################################
# Function to compute the Fourier frequencies.
Fourier_Freq<-function(n){
        Ln<- floor((n-1)/2) # this means take the integer part
        Un<-floor(n/2)
        Fn<- -Ln:Un
        omega<-2*pi*Fn/n
        return(omega)
}
##########################################################################
##########################################################################
##########################################################################
# Periodogram/(2*pi) function.
Pgram<-function(y){
        n<-length(y)
        Ln<- floor((n-1)/2) # this means take the integer part
        Un<-floor(n/2)
        Fn<- -Ln:Un
        # dft in R does not divide by n; need to do that here.
        #
        dft<-fft(y)/sqrt(n*2*pi)
        #
        # fft orders these (0,2pi) instead of (-pi,pi),
        # so (pi,2pi) needs to map to (-pi,0).
        #
        tmp<-dft
        dft[1:Ln]<-tmp[(Un+2):n]
        dft[(Ln+1):(Ln+Un+1)]<-tmp[1:(Un+1)]
        #
        I_y<-Re(dft*Conj(dft))
        return(I_y)
```

```
}
#########################################################################
#########################################################################
#########################################################################
fit_pspline<-function(I,omega,K=90,eps=0.005,penalty=1){
        # Need to delete frequency zero.
        zero<-(omega==0)
        I<-I[!zero]
        omega<-omega[!zero]
        knots<-log(eps)+(1:K)*(log(pi-eps)-log(eps))/K
        knots<-c(-rev(exp(knots)),exp(knots))
        ZZ<-outer(omega,knots,"-")
        ZZ<-ZZ*(ZZ>0)
        ZZ<-cbind(rep(1,length(omega)),omega,ZZ)
        fit<-solve(t(ZZ)%*%ZZ+diag(c(0,0,rep(penalty,2*K))))%*%t(ZZ)%*%cbind(log(I))
        return(fit)
}
#########################################################################
#########################################################################
#########################################################################
eval_pspline<-function(fit,omega,K=90,eps=0.005,penalty=1){
        knots<-log(eps)+(1:K)*(log(pi-eps)-log(eps))/K
        knots<-c(-rev(exp(knots)),exp(knots))
        ZZ<-outer(omega,knots,"-")
        ZZ<-ZZ*(ZZ>0)
        ZZ<-cbind(rep(1,length(omega)),omega,ZZ)
        eval<-ZZ%*%cbind(c(fit))
        return(eval)
}
#########################################################################
#########################################################################
#########################################################################
# Matrix of dft's.
DFT_Matrix<-function(y,Max_Lag){
   D<-c()
   N<-length(y)
    for(g in 0:Max_Lag){
                D<-cbind(fft(y[(g+1):(g+N-Max_Lag)]),D)
    }

   # Reorder D for consistency with periodogram.
   # fft orders these (0,2pi) instead of (-pi,pi),
   # so (pi,2pi) needs to map to (-pi,0).

   n<-N-Max_Lag
   Ln<- floor((n-1)/2) # this means take the integer part
   Un<-floor(n/2)
   tmp<-D
   D[1:Ln,]<-tmp[(Un+2):n,]
   D[(Ln+1):(Ln+Un+1),]<-tmp[1:(Un+1),]
   return(D)
}
#########################################################################
#########################################################################
#########################################################################
# Plot a criterion surface
Surface_Plot<-function(DT,phi,criterion){
        G<-length(DT)
        h<-topo.colors(G)
        plot(range(DT),range(phi),type="n",xlab="Split Time",ylab="Fast Axis")
        r<-rank(criterion)
        delta_DT<-max(diff(DT,1,1))
        delta_phi<-max(diff(abs(phi),1,1)) # can be messed up depending on order of grid values
```

```
	for(i in 1:G){
		rect(DT[i],phi[i],DT[i]+delta_DT,phi[i]+delta_phi,col=h[r[i]],border=NA)
	}# end loop on i
	g_max<-(1:G)[r==G]
	points(DT[g_max],phi[g_max],pch=17,col="red",cex=1.2)
}
#########################################################################
#########################################################################
#########################################################################
#Save the values of DT and phi in a list
Save_results<-function(DT,phi,criterion){
	G<-length(DT)
	r<-rank(criterion)
	g_max<-(1:G)[r==G]
	save<-list(DTm=DT[g_max],phim=phi[g_max])
	return(save)
}
#########################################################################
#########################################################################
#########################################################################
# Create lookup table using Menke and Levin one-layer functional forms.
# Change manually the maximum and minimum dt & maximun and minimum fast axis:
Lookup_Table<-
function(sqrt_G=200,scale=1,max_DT=4.0,min_DT=0,max_phi=180,min_phi=0,sample_interval=0.01,back_azimuth=baz){
	fast_axis<-rep((min_phi+((0:(sqrt_G-1))/sqrt_G)*(max_phi-min_phi)),sqrt_G)
	delta<-fast_axis-back_azimuth
	delta<-2*pi*delta/360
	DT<-sort(rep((min_DT+((0:(sqrt_G-1))/sqrt_G)*(max_DT-min_DT)),sqrt_G))
	R1<-scale*cos(delta)^2
	R2<-scale*sin(delta)^2
	T1<-scale*cos(delta)*sin(delta)
	T2<--T1
	Lag<-(DT/sample_interval)%/%1
	out<-list(fast_axis=fast_axis,DT=DT,R1=R1,R2=R2,T1=T1,T2=T2,Lag=Lag)
	return(out)
}
#########################################################################
#########################################################################
#########################################################################
# Set up manually the function SurrogateData from WaveletComp package
SurrogateData <-
function(x, method = "white.noise",
		params=list(AR     = list(p=1),
			ARIMA  = list(p=1, q=1, include.mean=T, sd.fac=1, trim = F, trim.prop = 0.01)
#			  ,
#			  meboot = list(trim = 0.1, force.clt = F, expand.sd = T, fiv = 5)
			)
		){

  if(method == "white.noise")  x.sur <- rnorm(length(x))
  if(method == "shuffle")      x.sur <- sample(x, length(x))
  if(method == "Fourier.rand") x.sur <- FourierRand(x)

  if(method == "AR")          {

    x.sur <- AR(x, params = params)

  }

#   if(method == "meboot")      {
#
#     trim      = params$meboot$trim
#     force.clt = params$meboot$force.clt
```

```
#     expand.sd = params$meboot$expand.sd
#     fiv       = params$meboot$fiv
#
#     x.sur <- meboot(x, reps=2, trim = trim, force.clt = force.clt, expand.sd = expand.sd, fiv = fiv)$ensemble[,1]
#
#   }

  if(method == "ARIMA")        {

     x.sur <- ARIMA(x, params = params)

  }

  return(invisible(x.sur))
}
## Code: Tian, H. and Cazelles, B., \code{WaveletCo}
#########################################################################
#########################################################################
#########################################################################
# Set up manually the function FourierRand from WaveletComp package
#Needed for using SurrogateData with the Fourier randomization method
FourierRand <-
function(x){
  n <- length(x)
  z <- fft(x)

  if(n%%2 == 0){
    ph <- 2*pi*runif(n/2-1)
    ph <- c(0, ph, 0, -rev(ph))}

  if(n%%2 != 0){
    ph <- 2*pi*runif((n-1)/2)
    ph <- c(0, ph, -rev(ph))}

  ph <- complex(imaginary = ph)
  z <- z * exp(ph)
  x.sur <- Re(fft(z, inverse = TRUE)/n)

  return(invisible(x.sur))
}
## Code: Tian, H. and Cazelles, B., \code{WaveletCo}
#########################################################################
#########################################################################
#########################################################################
## Requires several globally-defined variables: R1, R2, T1, T2, Outer_Real, Outer_Imag
## Evaluate log-like.
Whittle_fast<-function(DT,D_Rstar,D_Tstar,ln_f_R,ln_f_T,Omega,sample_interval=0.02){
    Max_Lag<-floor(4/sample_interval)
    N<-dim(D_Tstar)[1]
    SS<-(1:N)[Omega>0]
    lag<-DT/sample_interval
    Lag1<-floor(lag)
    ##
    ## Construct matrix with length(psi) rows and length(Omega) columns
    ## Vector is added to each column.
    rho2<-(R1^2+R2^2)+outer(2*R1*R2,cos(Lag1*Omega),"*")
    tau2<-(T1^2+T2^2)+outer(2*T1*T2,cos(Lag1*Omega),"*")
    ##
    ## Construct matrix of spectra for cross-convolved series.
    spectrum_cross1<-t(t(rho2)*c(exp(ln_f_T))+t(tau2)*c(exp(ln_f_R)))
    tmp_real<-Outer_Real+outer(R2,Re(D_Tstar[,Lag1+1]),"*")-outer(T2,Re(D_Rstar[,Lag1+1]),"*")
    tmp_imag<-Outer_Imag+outer(R2,Im(D_Tstar[,Lag1+1]),"*")-outer(T2,Im(D_Rstar[,Lag1+1]),"*")
    I_cross1<-(tmp_real^2+tmp_imag^2)/(2*pi*N)
```

```
    Lag2<-Lag1+1
    I_cross2<-0
    spectrum_cross2<-1
    like2<-rep(0,length(psi))
    if(lag>Lag1){
       tmp_real<-Outer_Real+outer(R2,Re(D_Tstar[,Lag2+1]),"*")-outer(T2,Re(D_Rstar[,Lag2+1]),"*")
       tmp_imag<-Outer_Imag+outer(R2,Im(D_Tstar[,Lag2+1]),"*")-outer(T2,Im(D_Rstar[,Lag2+1]),"*")
       I_cross2<-(tmp_real^2+tmp_imag^2)/(2*pi*N)
       rho2<-(R1^2+R2^2)+outer(2*R1*R2,cos(Lag2*Omega),"*")
       tau2<-(T1^2+T2^2)+outer(2*T1*T2,cos(Lag2*Omega),"*")
       ##
       ## Construct matrix of spectra for cross-convolved series.
       spectrum_cross2<-t(t(rho2)*c(exp(ln_f_T))+t(tau2)*c(exp(ln_f_R)))
       like2<-apply(-(I_cross2/spectrum_cross2)-log(spectrum_cross2),MAR=1,FUN="sum")
    }# end if lag
    ##
    like1<-apply(-(I_cross1/spectrum_cross1)-log(spectrum_cross1),MAR=1,FUN="sum")
    log_like<-(Lag2-lag)*like1+(lag-Lag1)*like2
    ##
    ##
    return(log_like)
}

#########################################################################
#########################################################################
#########################################################################
estimate_S_star<-function(Rstar,Tstar,L=120,rho=c(cos(pi/9)^2,sin(pi/9)^2),tau=c(cos(pi/9)*sin(pi/9),-cos(pi/9)*sin(pi/9))){
  N<-length(Rstar)
  Z_R<-matrix(0,N,N+L)
  Z_T<-matrix(0,N,N+L)

  tmp1<-cbind(matrix(0,N,L),diag(rep(rho[1],N)))
  tmp2<-cbind(diag(rep(rho[2],N)),matrix(0,N,L))
  Z_R<-tmp1+tmp2

  tmp1<-cbind(matrix(0,N,L),diag(rep(tau[1],N)))
  tmp2<-cbind(diag(rep(tau[2],N)),matrix(0,N,L))
  Z_T<-tmp1+tmp2

  YT<-cbind(Tstar)
  YR<-cbind(Rstar)
  Y<-rbind(YR,YT)
  Z<-rbind(Z_R,Z_T)
  S_star_hat<-lm(Y~-1+Z)$coef # estimate of the pre-processed signal, (1-B)S_t/sigma
  return(S_star_hat)
}
###
```

APPENDIX B

```
## Cross-convolution shear wave splitting code
## Implements new statistical assessment of splitting measurements via random-phase microseismic noise and
bootstrapping
## Authors: Dr. F. Jay Breidt, Ana Corbalan, and Derek Witt
## Last Edited: SEPT 2017 - Derek Witt

################ First, source latest version of Step_1_Setup.R ###################
library(foreach) # foreach package installation is needed.
library(doParallel) # doParallel package installation is needed. It is a "parallel backend" for the foreach package using the
%dopar% function. By default, doParallel uses multicore functionality on Unix-like systems and snow functionality on
Windows.
num_cores<-1
registerDoParallel(cores=num_cores)# setup multi-core cluster

starttime<-Sys.time()

## 1ST.- Calculate the estimated values of {DT,phi} for a many events with known BAZ and sum likelihoods
#########################################################################################################
######################
#########################################################################################################
######################

## Set up station/event pairs to iterate through
pathname<-"<INSERT PATHNAME>"
setwd(pathname)

stations<-read.table(paste(pathname,"<INSERT TEXT FILE LIST OF STATIONS>",sep=""))
S<-dim(stations)[1]
for (s in 1:S){

## Loop over stations
st<-stations[s,]

## The list(s) of events need to be made prior to running code
events<-read.table(paste(pathname, st, "_events.txt",sep=""))
E<-dim(events)[1]

setwd(paste(pathname,st,sep=""))

## Set up vectors of event-specific arrays
like_presum<-c()
bazvec<-c()
Ri_p<-c()
Ti_p<-c()
ln_f_Ri<-c()
ln_f_Ti<-c()
bazphi<-c()
bazdt<-c()

for (e in 1:E){

  ## Input event name, use consistent nomenclature for event naming
  event_name<-c(paste(events[e,]))
  Rsacfile<-rsac(paste(events[e,],".BHR.sac",sep=""), endian = .Platform$endian)
  Tsacfile<-rsac(paste(events[e,],".BHT.sac",sep=""), endian = .Platform$endian)

  ## Get the back azimuth from the sac file
```

```
  bazvec<-cbind(bazvec,Rsacfile[[1]]$baz)

  ## Get the sampling interval from the sac file, calculate sqrt_G which is used to set up integer lag
  si<- round(as.numeric(Rsacfile[[1]]$dt),3)
  sqrt_G<-4/si

  ## Create lookup table of fast axis and split time parameters
  lu<-Lookup_Table(sqrt_G=sqrt_G, sample_interval=si,back_azimuth=bazvec[,e])

  ## Setup R and T sac files
  Rsacfile<-Rsacfile[[1]]$amp
  Tsacfile<-Tsacfile[[1]]$amp

  ## Cut off some initial and some final values,
  ## then split into pre-SKS event (noise) and SKS event (signal plus noise)
  top<-length(Rsacfile)-1
  cut<-round(top/10) # may have to adjust "cut" intervals based on sample interval (8 is ideal for 50 Hz data, 10-16 for 20 Hz
data)
  R<-Rsacfile[cut:(top-cut)] # set up the length manually to get the pre-SKS noise and the SKS signal
  T<-Tsacfile[cut:(top-cut)] # set up the length manually to get the pre-SKS noise and the SKS signal
  mid<-round((top-cut-cut)/2)

  ##########################################################################################################
######################

  Ri<-R[1:mid] # Radial pre-SKS noise
  Ti<-T[1:mid] # Tangential pre-SKS noise

  outi<-preprocess(Ri,Ti,difference=TRUE)

  Ri_p<-cbind(Ri_p,outi$R)
  Ti_p<-cbind(Ti_p,outi$T)

  ni<-length(Ri_p[,e])
  omegai<-Fourier_Freq(ni)

  I_Ri<-Pgram(Ri_p[,e])
  fit_Ri<-fit_pspline(I_Ri,omegai,penalty=0.5)
  #omi<-omegai[omegai>0]
  #ln_f_Ri<-eval_pspline(fit_Ri,omi,penalty=0.5)

  I_Ti<-Pgram(Ti_p[,e])
  fit_Ti<-fit_pspline(I_Ti,omegai,penalty=0.5)
  #ln_f_Ti<-eval_pspline(fit_Ti,omi,penalty=0.5)

  ##########################################################################################################
######################

  Rstari<-R[(mid+1):(top-cut-cut)] # Radial SKS signal
  Tstari<-T[(mid+1):(top-cut-cut)]  # Tangential SKS signal

  out_stari<-preprocess(Rstari,Tstari,sigma=outi$sigma,difference=TRUE)
  Rstari_p<-out_stari$R
  Tstari_p<-out_stari$T
  MLagi<-max(lu$Lag)
  Ni<-length(Rstari_p)-MLagi
  Omegai<-Fourier_Freq(Ni)

  ln_f_Ri<-cbind(ln_f_Ri,eval_pspline(fit_Ri,Omegai,penalty=0.5))
  ln_f_Ti<-cbind(ln_f_Ti,eval_pspline(fit_Ti,Omegai,penalty=0.5))

  ##########################################################################################################
######################
```

```
  D_Rstari<-DFT_Matrix(Rstari_p,Max_Lag=MLagi)
  D_Tstari<-DFT_Matrix(Tstari_p,Max_Lag=MLagi)

  ##############################################################################################################
######################

  ## Vectorized Whittle set-up
  phi<-sort(unique(lu$fast_axis))-bazvec[,e]
  psi<-2*pi*phi/360 # convert to radians
  R1<<-cos(psi)^2
  R2<<-sin(psi)^2
  T1<<-cos(psi)*sin(psi)
  T2<<--T1
  Delta_T<-sort(unique(lu$DT))
  Outer_Real<<-outer(R1,Re(D_Tstari[,1]),"*")-outer(T1,Re(D_Rstari[,1]),"*")
  Outer_Imag<<-outer(R1,Im(D_Tstari[,1]),"*")-outer(T1,Im(D_Rstari[,1]),"*")


  Gi<-length(unique(lu$DT))

  # Whittle Grid Search
  likevi<-c()
  for(g in 1:Gi){
   likevi<-
c(likevi,Whittle_fast(Delta_T[g],D_Rstar=D_Rstari,D_Tstar=D_Tstari,ln_f_R=ln_f_Ri[,e],ln_f_T=ln_f_Ti[,e],Omega=Omegai,s
ample_interval=si))
  }

  # likevi_par<-foreach(g=1:Gi) %dopar% {
  #   out<-
Whittle_fast(Delta_T[g],D_Rstar=D_Rstari,D_Tstar=D_Tstari,ln_f_R=ln_f_Ri[,e],ln_f_T=ln_f_Ti[,e],Omega=Omegai,sample_i
nterval=si)
  # }
  # likevi<-c(likevi,unlist(likevi_par))

  ## Smooth likelihood surface for roughness in the DT dimension
  x <- unique(lu$DT)   # Get unique DT values
  L <- matrix(likevi,sqrt_G,sqrt_G)  # Put likei into a matrix
  L_smoother <- apply(L,MAR=1,FUN=smooth.spline,x=x,spar=0.6) # Apply smooth.spline to DT values
  tmp<-c()   # Loop through all fast axis directions to smooth DT
  for (i in 1:sqrt_G){
    tmp <- c(tmp,L_smoother[[i]]$y)
  }
  smooth_likevi<-c(t(matrix(tmp,sqrt_G,sqrt_G))) # Surface comes out flipped so take the transpose...

  ## Create matrix of individual likelihoods to sum
  like_presum<-cbind(like_presum,c(smooth_likevi))

  ## save baz vs fast axis and split time for each event
  tmp<-Save_results(lu$DT,lu$fast_axis,smooth_likevi)
  bazphi<-rbind(bazphi,cbind(bazvec[,e],tmp$phim))
  bazdt<-rbind(bazdt,cbind(bazvec[,e],tmp$DTm))
} ## End of likelihood calculation


## Sum likelihood surfaces to get final estimate
final_like<-apply(like_presum,MAR=1,FUN=sum)

## Plot and save results

pdf(paste(pathname,st,'_log_likelihood.pdf',sep=""))
Surface_Plot(lu$DT,lu$fast_axis,final_like)
title(main=paste("Log-Likelihood for ",st))
```

```
dev.off()

save<-Save_results(lu$DT,lu$fast_axis,final_like)
est_DT<-c(round(save$DTm,3)) # estimated value of DT with the code based on the cross-convolution method
est_phi<-c(round(save$phim,2)) # estimated value of phi with the code based on the cross-convolution method

list<-cbind(est_DT,est_phi)

## Save splitting parameters, fast axis vs. baz, and split time vs. baz
write.table(list, file=(paste(pathname,st,'_splitting_results.txt',sep="")), sep="\t", row.names=FALSE, col.names=FALSE)
write.table(bazphi, file=(paste(pathname,st,'_baz_vs_fast_axis.txt',sep="")), sep="\t", row.names=FALSE,
col.names=FALSE)
write.table(bazdt, file=(paste(pathname,st,'_baz_vs_split_time.txt',sep="")), sep="\t", row.names=FALSE,
col.names=FALSE)

##########################################################################################################
######################
##########################################################################################################
######################
##########################################################################################################
######################

## 2ND.- Create synthetic signal, radial, and transverse seismograms with the estimated values of {DT,phi} calculated on
the 1st step
##########################################################################################################
######################
##########################################################################################################
######################

# Set up earth model parameters
split_time<-est_DT
fast_axis<-est_phi
Lag<-floor(split_time/si) # integer lag based on sample interval

# Set up event-specific arrays that need to be filled after initial estimate
top_angle<-c()
Rho1<-c()
Rho2<-c()
Tau1<-c()
Tau2<-c()
Rsig<-c()
Tsig<-c()
Rstar_in<-c()
Tstar_in<-c()
St<-c()

# Loop through event list to populate arrays

for (e in 1:E){

  # Find angle between fast axis and baz in radians
  top_angle_degrees<-fast_axis-bazvec[,e] # angle between fast axis and baz in top layer
  top_angle<-cbind(top_angle,2*pi*top_angle_degrees/360)

  # Set up the amplitudes of impulses (from Levin and Menke)

  Rho1<-cbind(Rho1,cos(top_angle[,e])^2)
  Rho2<-cbind(Rho2,sin(top_angle[,e])^2)
  Tau1<-cbind(Tau1,cos(top_angle[,e])*sin(top_angle[,e]))
  Tau2<-cbind(Tau2,-Tau1[,e])

  # Set up R and T components for least-square regression for source signal estimation
  Rsig<-cbind(Rsig,R[-1])
```

```
  Tsig<-cbind(Tsig,T[-1])

  # Estimate the true signal that produced the data to use it as the input wavelet
  true_signal<-estimate_S_star(Rsig[,e],Tsig[,e],L=Lag,rho=c(Rho1[,e],Rho2[,e]),tau=c(Tau1[,e],Tau2[,e]))
  St<-cbind(St,c(rep(0,cut+Lag),true_signal,rep(0,cut-Lag))) # Make the estimated signal the same length as the input
seismograms + integer Lag, fill beginning and end with zeros

  # Convolve Menke and Levin coefficients with estimated source signal
  RDATA<-rep(0,top)
  TDATA<-RDATA

  for(i in (Lag+1):(top+Lag)){
    RDATA[i-Lag]=Rho1[,e]*St[i,e]+Rho2[,e]*St[i-Lag,e]
    TDATA[i-Lag]=Tau1[,e]*St[i,e]+Tau2[,e]*St[i-Lag,e]
  }


  # Cut and scale the signal to the same length and same variance as the real signal (Rstari)
  Rboot<-RDATA[cut:(top-cut)]
  Tboot<-TDATA[cut:(top-cut)]

  Rstar_in<-cbind(Rstar_in,Rboot[(1+mid):(top-cut-cut)])
  Tstar_in<-cbind(Tstar_in,Tboot[(1+mid):(top-cut-cut)])

}


## 3RD.- Bootstrapping the code with the synthetic noise free seismogram created on the 2nd step and the noise file from
1st step
# Set up bootstrapping

B<-100 # Bootstrap iterations

##########################################################################################################
#####################
##########################################################################################################
#####################
# LOOP STARTS HERE
# Loop over the code to get the values of DT and phi for different repeated simulations of synthetic data foreach iterates
over the variables in parallel

bootstart<-Sys.time()

  # Set up c vectors
  Rb_p<-c()
  R2b_p<-c()
  Tb_p<-c()
  T2b_p<-c()
  Rb_up<-c()
  R2b_up<-c()
  Tb_up<-c()
  T2b_up<-c()

  results<-c()
  indresults<-c()
  likev_presum<-c()
  final_likev<-c()

  # Results<-foreach(i=1:ncol(Rb_up), j=1:ncol(Tb_up), k=1:ncol(R2b_up), l=1:ncol(T2b_up)) %dopar% {

  for(b in 1:B){
  #Results<-foreach(b=1:B) %dopar% {
    likev_presum<-c()
```

```
  final_likev<-c()
  for(e in 1:E){

  ## Generate random-phase noise surrogated from pre-SKS arrival noise
  Rb_p<-c(SurrogateData(Ri_p[,e], method = "Fourier.rand"))
  R2b_p<-c(SurrogateData(Ri_p[,e], method = "Fourier.rand"))

  Tb_p<-c(SurrogateData(Ti_p[,e], method = "Fourier.rand"))
  T2b_p<-c(SurrogateData(Ti_p[,e], method = "Fourier.rand"))

  out<-unpreprocess(Rb_p,Tb_p,Sigma=outi$sigma,undifference=TRUE)
  Rb_up<-c(out$R)
  Tb_up<-c(out$T)

  out<-unpreprocess(R2b_p,T2b_p,Sigma=outi$sigma,undifference=TRUE)
  R2b_up<-c(out$R)
  T2b_up<-c(out$T)

  ##########################################################################################################
########################

  out<-preprocess(Rb_up,Tb_up,difference=TRUE)
  R_out<-out$R
  T_out<-out$T
  n<-length(R_out)
  omega<-Fourier_Freq(n)
  I_R<-Pgram(R_out)
  fit_R<-fit_pspline(I_R,omega,penalty=0.5)
  om<-omega[omega>0]
  ln_f_R<-eval_pspline(fit_R,om,penalty=0.5)

  I_T<-Pgram(T_out)
  fit_T<-fit_pspline(I_T,omega,penalty=0.5)
  ln_f_T<-eval_pspline(fit_T,om,penalty=0.5)

  ##########################################################################################################
########################

  Rstar<-Rstar_in[,e] + R2b_up
  Tstar<-Tstar_in[,e] + T2b_up

  out_star<-preprocess(Rstar,Tstar,sigma=out$sigma,difference=TRUE)
  Rstar_out<-out_star$R
  Tstar_out<-out_star$T
  MLag<-max(lu$Lag)
  N<-length(Rstar_out)-MLag
  Omega<-Fourier_Freq(N)

  ln_f_R<-eval_pspline(fit_R,Omega,penalty=0.5)
  ln_f_T<-eval_pspline(fit_T,Omega,penalty=0.5)

  ##########################################################################################################
########################

  D_Rstar<-DFT_Matrix(Rstar_out,Max_Lag=MLag)
  D_Tstar<-DFT_Matrix(Tstar_out,Max_Lag=MLag)

  ##########################################################################################################
########################
  ## Vectorized Whittle approximation set-up
  phi<-sort(unique(lu$fast_axis))-bazvec[,e]
  psi<-2*pi*phi/360 # convert to radians
  R1<<-cos(psi)^2
```

```
  R2<<-sin(psi)^2
  T1<<-cos(psi)*sin(psi)
  T2<<--T1
  Delta_T<-sort(unique(lu$DT))
  Outer_Real<<-outer(R1,Re(D_Tstar[,1]),"*")-outer(T1,Re(D_Rstar[,1]),"*")
  Outer_Imag<<-outer(R1,Im(D_Tstar[,1]),"*")-outer(T1,Im(D_Rstar[,1]),"*")

  ##########################################################################################################
########################

  Gi<-length(unique(lu$DT))
  ## like<-rep(0,G)
  #SS<-(1:N)[Omega>0]
  likev<-c()
  for(g in 1:Gi){
   likev<-
c(likev,Whittle_fast(Delta_T[g],D_Rstar=D_Rstar,D_Tstar=D_Tstar,ln_f_R=ln_f_Ri[,e],ln_f_T=ln_f_Ti[,e],Omega=Omegai,sa
mple_interval=si))
  }
  # likev_par<-foreach(g=1:Gi) %dopar% {
  #   out<-
Whittle_fast(Delta_T[g],D_Rstar=D_Rstari,D_Tstar=D_Tstari,ln_f_R=ln_f_Ri[,e],ln_f_T=ln_f_Ti[,e],Omega=Omegai,sample_i
nterval=si)
  # }
  # #
  # likev<-c(likev,unlist(likev_par))

  ##########################################################################################################
########################
  ## Smooth 3D likelihood surface in DT dimension for each bootstrap replicate

  x <- unique(lu$DT)   # Get unique DT values
  L_b <- matrix(likev,sqrt_G,sqrt_G)  # Put likei into a matrix
  L_smoother_b <- apply(L_b,MAR=1,FUN=smooth.spline,x=x,spar=0.6) # Apply smooth.spline to DT values

  tmp<-c()   # Loop through all fast axis directions to smooth DT
  for (i in 1:sqrt_G){
    tmp <- c(tmp,L_smoother_b[[i]]$y)
  }

  smooth_likev<-c(t(matrix(tmp,sqrt_G,sqrt_G))) # Surface comes out flipped so take the transpose...

  # Save every station-event bootstrapping result
  saveind<-Save_results(lu$DT,lu$fast_axis,smooth_likev)
  indresults<-rbind(indresults,c(save$DTm,save$phim))

  # Save pre-summed bootstrapping likelihoods
  likev_presum<-cbind(likev_presum,c(smooth_likev))

  } # end of event loop

  final_likev<-cbind(final_likev,apply(likev_presum,MAR=1,FUN=sum))

  # save<-Save_results(lu$DT,lu$fast_axis,final_likev[,b])
  save<-Save_results(lu$DT,lu$fast_axis,final_likev)
  results<-rbind(results,c(save$DTm,save$phim))

  #Results<-matrix(data=Results,nrow=B,ncol=2)
  #Results[b,]<-c(results)

  ##########################################################################################################
########################
```

```
  ##########################################################################################################
#######################
  ##########################################################################################################
#######################

 } # end of bootstrap loop

#} #dopar
 # Calculate stats for summed and unsummed likelihood realizations
 bootdtsd<-sd(results[,1])
 bootphisd<-sd(results[,2])
 indbootdtsd<-sd(indresults[,1])
 indbootphisd<-sd(indresults[,2])
 # bootdtmean<-mean(results[,1])
 # bootphimean<-mean(results[,2])
 # indbootdtmean<-mean(indresults[,1])
 # indbootphimean<-mean(indresults[,2])
 bootstats<-cbind(bootdtsd,bootphisd)
 indbootstats<-cbind(indbootdtsd,indbootphisd)
 stats<-cbind(est_DT,est_phi,indbootstats)

 #Results<-t(round(matrix(unlist(Results),2,B),2))
 write.table(results, file=(paste(pathname,st,'_bootstrapping_results.txt',sep="")), sep="\t", row.names=FALSE,
col.names=FALSE)
 write.table(indresults, file=(paste(pathname,st,'_stationevent_bootstrapping_results.txt',sep="")), sep="\t",
row.names=FALSE, col.names=FALSE)
 write.table(stats, file=(paste(pathname,st,'_results_stats.txt',sep="")), sep="\t", row.names=FALSE, col.names=FALSE)
 boottime<-Sys.time()-bootstart
} #end of station loop (if being used)
totaltime<-Sys.time()-starttime
```

APPENDIX C

```
<!--SOD recipe that specializes in SKS data aquisition and pre-processing-->

<?xml version="1.0"?>
<sod>

<!-- ================== Event Arm ================== -->
   <eventArm>

      <fdsnEvent>
         <originTimeRange>
            <startTime>
               1985-01-01T00:00:00.000Z    <!-- insert desired date range -->
            </startTime>
            <endTime>
               <now/>
            </endTime>
         </originTimeRange>

         <magnitudeRange>
            <magType>mww</magType>
            <min>5.8</min>
            <max>10</max>
         </magnitudeRange>
      </fdsnEvent>

      <originOR>
         <originAND>
            <originDepthRange>
               <unit>KILOMETER</unit>
               <min>0</min>
               <max>10000</max>
            </originDepthRange>
         </originAND>
      </originOR>

      <removeEventDuplicate>
         <timeVariance>
            <unit>MINUTE</unit>
            <value>5</value>
         </timeVariance>
      </removeEventDuplicate>

      <printlineEventProcess>
         <template>$event.getLongitude('##0.0000;-##0.0000') $event.getLatitude('##0.0000;-##0.0000')
$event.getDepth('###0.##') ${event.getTime('yyyy_DDD_HH_mm_sss')}
$event.magnitudeValue$event.magnitudeType</template>
      </printlineEventProcess>

   </eventArm>

<!-- ================== Network Arm ================== -->
   <networkArm>

      <fdsnStation/>

      <networkOR><!--Accept any of these networks-->
         <networkCode>INSERT DESIRED NETWORK CODE HERE</networkCode>
      </networkOR>
```

```
      <stationAND>
         <stationBoxArea>
            <latitudeRange>      <!--Aribitrary lat/lon range -->
               <min>58</min>
               <max>70</max>
            </latitudeRange>
            <longitudeRange>
               <min>-145</min>
               <max>-110</max>
            </longitudeRange>
         </stationBoxArea>
      </stationAND>

      <channelAND> <!--Accept only Broadband and Highgain channels-->
         <bandCode>B</bandCode>
         <gainCode>H</gainCode>
      </channelAND>

      <printlineChannelProcess/>

   </networkArm>

<!-- ==================== Waveform Vector Arm ==================== -->
   <waveformVectorArm>

      <eventStationAND>
         <distanceRange>
            <unit>DEGREE</unit>
            <min>80</min>
            <max>125</max>
         </distanceRange>
         <phaseWithoutInterference>
            <phaseName>SKS</phaseName>
            <beginOffset>
               <unit>SECOND</unit>
               <value>-10</value>
            </beginOffset>
            <endOffset>
               <unit>SECOND</unit>
               <value>15</value>
            </endOffset>
            <interferingPhase>S</interferingPhase>
            <interferingPhase>ScS</interferingPhase>
            <interferingPhase>SKKS</interferingPhase>
            <interferingPhase>SKiKS</interferingPhase>
            <interferingPhase>PKS</interferingPhase>
            <interferingPhase>Sdiff</interferingPhase>
         </phaseWithoutInterference>
      </eventStationAND>
      <phaseRequest>
         <model>ak135</model>
         <beginPhase>SKS</beginPhase>
         <beginOffset>
            <unit>SECOND</unit>
            <value>-150</value>
         </beginOffset>
         <endPhase>SKS</endPhase>
         <endOffset>
            <unit>SECOND</unit>
            <value>100</value>
         </endOffset>
      </phaseRequest>
```

```
    <printlineRequest/> <!-- view request for debugging purposes -->
    <fdsnDataSelect/>
    <someCoverage/>
    <responseGain/>
    <rMean/>
    <rTrend/>

    <phaseCut>
      <model>ak135</model>
      <beginPhase>SKS</beginPhase>
      <beginOffset>
        <unit>SECOND</unit>
        <value>-50</value>
      </beginOffset>
      <endPhase>SKS</endPhase>
      <endOffset>
        <unit>SECOND</unit>
        <value>+50</value>
      </endOffset>
    </phaseCut>

    <threeComponentData/>
    <merge/>
    <vectorTrim/>
    <rotateGCP>
      <ninetyDegreeTol>5</ninetyDegreeTol>
    </rotateGCP>

    <ORWaveformProcessWrapper>
      <seismogramAND>
        <orientationCode>R</orientationCode>
        <phaseSignalToNoise>
          <phaseName>SKS</phaseName>
          <shortOffsetBegin>
            <unit>SECOND</unit>
            <value>-5</value>
          </shortOffsetBegin>
          <shortOffsetEnd>
            <unit>SECOND</unit>
            <value>10</value>
          </shortOffsetEnd>
          <longOffsetBegin>
            <unit>SECOND</unit>
            <value>-20</value>
          </longOffsetBegin>
          <longOffsetEnd>
            <unit>SECOND</unit>
            <value>-5</value>
          </longOffsetEnd>
          <ratio>2.5</ratio>
        </phaseSignalToNoise>
      </seismogramAND>
    </ORWaveformProcessWrapper>

    <sacWriter>
      <workingDir>raw_sac</workingDir>
      <location>${network.code}.${station.code}/${event.getTime('yyyyDDDHHmmss')}.${network.code}.${station.code}.${
channel.code}.sac</location>
      <phaseTimeHeader>
        <model>ak135</model>
        <phaseName>SKS</phaseName>
        <tHeader>0</tHeader>
      </phaseTimeHeader>
```

```
            <phaseTimeHeader>
               <model>ak135</model>
               <phaseName>S</phaseName>
               <tHeader>1</tHeader>
            </phaseTimeHeader>
            <phaseTimeHeader>
               <model>ak135</model>
               <phaseName>ScS</phaseName>
               <tHeader>2</tHeader>
            </phaseTimeHeader>
            <phaseTimeHeader>
               <model>ak135</model>
               <phaseName>SKKS</phaseName>
               <tHeader>3</tHeader>
            </phaseTimeHeader>
            <phaseTimeHeader>
               <model>ak135</model>
               <phaseName>SKiKS</phaseName>
               <tHeader>4</tHeader>
            </phaseTimeHeader>
            <phaseTimeHeader>
               <model>ak135</model>
               <phaseName>SKIKS</phaseName>
               <tHeader>5</tHeader>
            </phaseTimeHeader>
            <phaseTimeHeader>
               <model>ak135</model>
               <phaseName>Sdiff</phaseName>
               <tHeader>6</tHeader>
            </phaseTimeHeader>
         </sacWriter>

         <printlineSeismogramProcess>
            <filename>SOD_seismograms_SKS.log</filename>
            <template>Got $seismograms.size() seismograms, Event_${event.getTime('yyyy_DDD_HH_mm_ss')},
${event.latitude}, ${event.longitude}, ${event.depth}, ${station.codes}.${channel.code}, ${station.latitude},
${station.longitude}</template>
         </printlineSeismogramProcess>

      </waveformVectorArm>
   </sod>
```

APPENDIX D

Event (YYYYMMDD.HHMMSS) | Time Window (s) | List of stations requested
20101025.144222 1800 'CLVN DHRN DLBC FNBB FNBC LDBN PLBC ROMN SMPN'
20101025.193731 1800 'CLVN DHRN DLBC FNBB FNBC LDBN PLBC ROMN SMPN'
20101030.151833 1800 'CLVN DHRN DLBC FNBB FNBC LDBN PLBC ROMN SMPN'
20101202.031209 1800 'CLVN DHRN DLBC FNBB FNBC LDBN PLBC ROMN SMPN'
20101213.011442 1800 'CLVN DHRN DLBC FNBB FNBC LDBN PLBC ROMN SMPN'
20101220.184159 1800 'CLVN DHRN DLBC FNBB FNBC LDBN PLBC ROMN SMPN'
20101225.131637 1800 'CLVN DHRN DLBC FNBB FNBC LDBN PLBC ROMN SMPN'